

## BIOPHYSICS

# The emergence of spontaneous coordinated epithelial rotation on cylindrical curved surfaces

Alexandros Glentis<sup>1†</sup>, Carles Blanch-Mercader<sup>2†</sup>, Lakshmi Balasubramaniam<sup>1</sup>, Thuan Beng Saw<sup>3</sup>, Joseph d'Alessandro<sup>1</sup>, Sébastien Janel<sup>4</sup>, Audrey Douanier<sup>5</sup>, Benedicte Delaval<sup>5</sup>, Frank Lafont<sup>4</sup>, Chwee Teck Lim<sup>3,6,7</sup>, Delphine Delacour<sup>1</sup>, Jacques Prost<sup>2,3\*</sup>, Wang Xi<sup>1\*</sup>, Benoit Ladoux<sup>1\*</sup>

Three-dimensional collective epithelial rotation around a given axis represents a coordinated cellular movement driving tissue morphogenesis and transformation. Questions regarding these behaviors and their relationship with substrate curvatures are intimately linked to spontaneous active matter processes and to vital morphogenetic and embryonic processes. Here, using interdisciplinary approaches, we study the dynamics of epithelial layers lining different cylindrical surfaces. We observe large-scale, persistent, and circumferential rotation in both concavely and convexly curved cylindrical tissues. While epithelia of inverse curvature show an orthogonal switch in actomyosin network orientation and opposite apicobasal polarities, their rotational movements emerge and vary similarly within a common curvature window. We further reveal that this persisting rotation requires stable cell-cell adhesion and Rac-1-dependent cell polarity. Using an active polar gel model, we unveil the different relationships of collective cell polarity and actin alignment with curvatures, which lead to coordinated rotational behavior despite the inverted curvature and cytoskeleton order.

Copyright © 2022  
The Authors, some  
rights reserved;  
exclusive licensee  
American Association  
for the Advancement  
of Science. No claim to  
original U.S. Government  
Works. Distributed  
under a Creative  
Commons Attribution  
NonCommercial  
License 4.0 (CC BY-NC).

## INTRODUCTION

Whole-tissue collective epithelial rotation (CeR) features a cohort of cells lining a quadric surface, such as ellipsoid and sphere, persistently and synchronously rotating three-dimensionally (3D) around a given axis with no free edge. This unexpected behavior has been observed *in vivo* and *in vitro*. As a particular type of collective epithelial movement, CeR plays a critical role in embryonic development (1–4) and glandular tissue transformation (5), accompanies tissue morphogenesis (6), and may be involved in cancerous invasion (7). A marked example is a global follicle epithelial cell rotation around the long axis of the egg chamber, relative to and within the overlaying basement membrane, during *Drosophila* oogenesis (1–3). This rotation starts from stage one and lasts consistently for hours until later stages (2). Similarly, clusters of cells in the developing *Drosophila* genitalia rotate 24 hours after puparium formation (4). Besides these *in vivo* phenomena, mammary epithelial acini embedded in 3D hydrogel matrices also demonstrate coordinated rotational movement (6, 8), which may contribute to the establishment of acinar structures (5) and alveogenesis (6). These observations suggest that CeR could be an intrinsic, preserved property of curved epithelia (9). In addition, how dynamic epithelia interact with their underlying curvatures remains an intriguing question to better understand 3D active tissue mechanics.

Similar to other sorts of collective migration, cells could establish coordinated tissue-level front-to-rear polarity, such as actin-based

lamellipodial protrusions (2) and Rac-1 gradient (10), to maintain a persistent CeR. In an expanding 2D epithelium with a leading front, the monolayer is facing an open space. The leader cells constantly sense the presence of a “front” edge and a “rear” edge via intercellular cadherin adhesions (11). This leads to a mechanosensing pathway gradient not only in the leaders but also spanning tens of cells behind (12). In contrast, cells within a rotating tissue have no free edges, and there is no inherent “forward” direction. Thus, the well-established mechanism for a canonical leader-guided collective migration may not be entirely applicable. In a rotating epithelium, each cell is surrounded by others and, in principle, behaves as a follower cell. Under this circumstance, recent investigations have shown that cells within an intact, migrating epithelium are also polarized and actively orient and contribute to directional collective migration (13, 14). Lacking information as to the position of leader cells, these cells may rely more on anisotropic cell-cell interactions to align their front-rear polar axes (9, 11). These include force-induced collective tissue polarity (12, 15, 16) that may originate from anisotropic mechanical stresses, tension, and tugging at the cell cortex. These mechanical signals can be propagated through actin cytoskeleton network and lateral cell-cell adhesions (17). Hence, perturbation of actin organization and cell-cell adhesion may compromise symmetry breaking in an intact epithelium and hamper its directional collective motility. In previous works using 3D epithelial acini, molecular analysis reveals a relationship between coordinated rotation and actin polymerization, cell-cell adhesion, and cell apical-basal polarity (5, 8). In addition, during *Drosophila* oogenesis (1–3), circumferentially aligned actin filaments lining the inner surface of the follicular epithelium are found to aid the persisting azimuthal rotation (1, 2, 18). In parallel, this global rotation of follicle cells is coupled to the maintenance of actin stress fiber (SF) alignment, lamellipodial protrusions, and remodeling of the extracellular matrix (ECM) (2).

In light of the above notions and considering CeR occurs on quadric surfaces, it is then rational to deduce that CeR might be a geometry-sensitive behavior. In addition, actin filaments in cells are

<sup>1</sup>Université Paris Cité, CNRS, Institut Jacques Monod, F-75013 Paris, France. <sup>2</sup>Laboratoire Physico Chimie Curie, UMR 168, Institut Curie, PSL Research University, CNRS, Sorbonne Université, 75005 Paris, France. <sup>3</sup>Mechanobiology Institute, National University of Singapore, 5A Engineering Drive 1, Singapore 117411, Singapore. <sup>4</sup>Univ. Lille, CNRS, Inserm, CHU Lille, Institut Pasteur Lille, U1019–UMR 9017–CIL–Center for Infection and Immunity of Lille, F-59000 Lille, France. <sup>5</sup>CRBM, Univ Montpellier, CNRS, Montpellier, France. <sup>6</sup>Department of Biomedical Engineering, National University of Singapore, 4 Engineering Drive 3, Singapore 117583, Singapore. <sup>7</sup>Institute for Health Innovation and Technology, National University of Singapore, 14 Medical Drive, Singapore 117599, Singapore.

\*Corresponding author. Email: jacques.prost@curie.fr (J.P.); wang.xi@ijm.fr (W.X.); benoit.ladoux@ijm.fr (B.L.)

†These authors contributed equally to this work.

sensitive to geometries and are known to reorient and reorganize in response to 2D patterns (19) and substrate curvatures (20–22). Actin cytoskeleton remodeling and nematic ordering (23) have been shown to be implicated in cellular mechanosensing either experimentally (24) or theoretically (25–27). Thus, concavely curved tissues could have radically different actomyosin network organization from that in convexly bent tissues. These changes could elicit variations in cell-cell/cell-substrate interactions, thereby affecting tissue rotational movement (1, 8, 28). Given the aforementioned example of *Drosophila* egg chambers, it is intuitive to envision that the polarized, circumferentially aligned actin networks may facilitate anisotropic force transition via cell-cell adhesions. This could promote collective polarity and CeR along the principal stress direction as in planar epithelia (29). However, the relationship between actin cytoskeleton network and directional CeR remains elusive until now. In addition, it is not immediately clear whether CeR is correlated with polarized actomyosin network organization and/or cell-cell adhesion, which may link to asymmetric mechanical tension transmission in a tissue. A recent 2D patterned model has revealed that the maintenance of collective rotation without a leading front requires polarity signals at the single-cell level rather than stable cell-cell junctions (CCJs) (10). Furthermore, current studies used exclusively concavely curved ellipsoidal or spherical epithelia with a central, apical lumen, such as a handful of *in vivo* (e.g., *Drosophila* egg) or 3D culture (e.g., acini and organoids in 3D hydrogels) models. This overlooks the possibility and potential consequences of reverse apicobasal and actin polarized structures and other complexities because of changes in curvatures. Controllable geometric cues are then necessary to unravel the intertwined relationship among actin alignment, cell-cell adhesion, cell polarity, curvatures, and CeR. Hence, exploring collective cell dynamics as a function of curved environments will improve our understanding of tissue behaviors under complicated geometrical conditions *in vivo* and *in vitro*.

In this study, we ask whether CeR is merely a geometry-dependent behavior or a wider phenomenon that manifests itself as an intrinsic property of epithelial tissues whenever the context allows. We use microfabricated tubes and fibers as simple and define cylindrical substrates for cell culture. To address the abovementioned questions and acquire deep insights into CeR dynamics on cylindrical curvatures, we form concavely (negatively) and convexly (positively) curved epithelial monolayers. We find that epithelial cells can self-organize to display whole-tissue-level persistent rotation over a large range of curvatures. Using an active polar fluid framework, we explore the rotational dynamics on various curvatures with opposite nematic orders in actin cytoskeleton.

## RESULTS

### Whole-tissue level rotation in 3D concave cylindrical epithelia

Persistent rotation around a random axis in spherical cysts (acini; fig. S1A) of Madin-Darby canine kidney (MDCK) cells embedded in hydrogel matrices has been reported previously (5, 8, 28). Such a culture approach is often used to recapitulate epithelial tubular morphogenesis (30, 31) and tube-shaped tissues (ducts; Fig. 1A and fig. S1B) with apically polarized cells facing a central lumen. To facilitate cell tracking, we used MDCK histone 1-green fluorescent protein (H1-GFP) cells. We formed MDCK acini and ducts of varying sizes and closed topologies that are ranging from 25 to 75  $\mu\text{m}$  in

diameter ( $\emptyset$ ) and up to 400  $\mu\text{m}$  in length. In both types of MDCK tissues, we observed persistent CeR (Fig. 1B; fig. S1, C and D; and movies S1 and S2) when mitosis was ceased by mitotic inhibitor mitomycin C. This is reminiscent of the fast rotation phase in *Drosophila* oogenesis when follicle cells cease division (2, 32). Elimination of mitosis may promote CeR as mitotic stresses (33) can disturb directed collective migration in confined space (21). Although collective cell rotation happened in both MDCK acini and ducts, their behaviors were different. In contrast to acini whose rotational axis varied in time, rotating MDCK ducts (up to  $\emptyset = 75 \mu\text{m}$ ) moved around a defined longitudinal ( $l$ ) axis (fig. S1E). This resulted in parallel cell trajectories along the cylindrical azimuthal ( $a$ ) direction (Fig. 1, B and C). This spontaneous movement had a characteristic nonzero, relatively stable average azimuthal velocity,  $V_\theta$ , over time and a close-to-zero, fluctuating average longitudinal velocity,  $V_z$  (Fig. 1, C and D). These features indicate that epithelial ducts could establish collective circumferential rotation even when movement in the longitudinal direction was allowed. In this work, we then examined the coordinated rotation of cylindrical tissues (CTs) around a defined  $l$  axis with  $|V_\theta| > 0$  and  $|V_z| \approx 0$ , which persisted for at least 3 hours. In addition, we also found short-period CeR in pronephric tubules of developing zebrafish embryos of 35 hours post-fertilization (hpf) (movie S3 and fig. S1, F and G) (34). Cells in the elongating epithelial tubules also demonstrated persistent azimuthal movements for hours around the  $l$  axis with slightly lower velocities than those of Matrigel-embedded MDCK ducts and MDCK CTs in polydimethylsiloxane (PDMS) microtubes (see next paragraph) of similar size (fig. S1H).

These observations inspired us to further investigate the emergence of CeR in epithelial monolayers with a concave cylindrical shape. To simplify the geometrical complexity of the self-organizing ducts, we used an established approach (21) and grew MDCKs into confluent tubular tissues inside PDMS microtubes (fig. S2A). This method allowed us to form well-defined concave MDCK tubes ranging from 25 to 250  $\mu\text{m}$  in diameter and up to 1000  $\mu\text{m}$  in length (Fig. 1E and fig. S2B). In addition, the MDCK tubular CTs ( $t$ -CTs) enclosed a hollow lumen and showed an apicobasal polarity toward the lumen (fig. S2C), reminiscent of follicle epithelial polarity (2, 35) and MDCK ducts (Fig. 1A and fig. S1B). Notably, we observed persistent CeR around the  $l$  axis (movie S4) in both clockwise and counterclockwise directions (Fig. 1F). These coordinated motions as disclosed by the angular displacement of cells (Fig. 1G) occurred in more than 60% of  $t$ -CTs of all different MDCK cell types tested, spanning from 25  $\mu\text{m}$  (smallest size possible) to 150  $\mu\text{m}$  in diameter (Fig. 1H) and persisting up to 40 hours (Fig. 1G). Moreover, we observed similar CeR behaviors inside fibronectin-/Matrigel-/poly-L-lysine-coated (fig. S3) PDMS microtubes. These observations suggested that CeR may not be sensitive to ECM components although substrate coating could be modified by cell-induced reorganization of the matrix (36).

### Characteristics of epithelial tissue rotation inside microtubes

To analyze the collective rotational dynamics, we virtually opened the  $t$ -CTs using a home-built Fiji macro (see Materials and Methods) (21), which allowed us to convert 3D movies into 2D projections (Fig. 2A). In typical 2D projections of rotating  $t$ -CTs, individual cell trajectories were mostly parallel to the azimuthal axis ( $a$  axis; Fig. 2B). Particle imaging velocimetry (PIV) analysis on these 2D

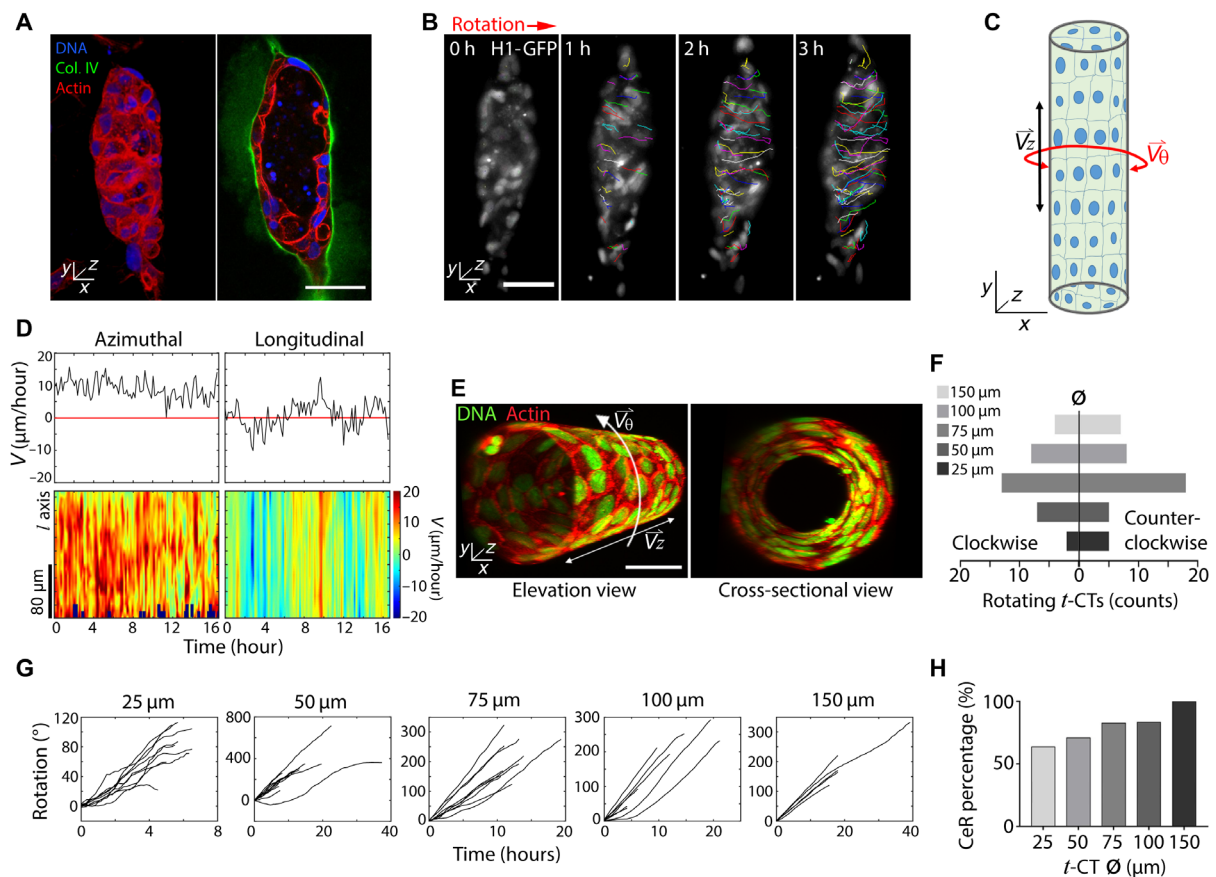


**Fig. 1. Whole-tissue collective rotation in 3D concave cylindrical epithelia.** (A) Images of a histone 1-GFP (H1-GFP) MDCK duct inside Matrigel at different z positions. Left, view from top; right, cross-sectional view, revealing hollow lumen inside the structure. H1-GFP nuclei are colored in blue, actin (phalloidin) in red, and collagen type IV (Col. IV) in green. (B) Time-lapsed images showing the circumferential rotation of the MDCK duct from (A). Single-cell trajectories are shown as varying colored lines. Red arrow indicates the rotational direction. (C) Schematic representation of a confluent MDCK tubular CT (t-CT) with collective movements with longitudinal ( $\vec{V}_z$ ) and azimuthal ( $\vec{V}_\theta$ ) velocities. The symbols were used to match the conventional terminology to describe a cylindrical system. (D) Graphs (top) and kymographs (bottom) displaying the average velocities ( $V$ ) of the MDCK duct from (A) in azimuthal and longitudinal directions as a function of time.  $V$  is calculated using particle imaging velocimetry (PIV) analysis. The graphs then plot the average azimuthal and longitudinal component of  $V$  for each time point, reflecting the average movement of the whole duct. The kymographs demonstrate spatial average  $\vec{V}_\theta$  and  $\vec{V}_z$  along the  $l$  axis for every time point for the entire observation period, thus showing spatiotemporal distribution of local velocities. (E) Representative 3D reconstructed images of an MDCK t-CT with  $\emptyset = 100 \mu\text{m}$ . Actin, red; nuclei, green (H1-GFP). White arrows show either  $\vec{V}_\theta$  or  $\vec{V}_z$ . (F) Graphs representing counts of clockwise and counterclockwise rotating t-CTs of varying diameters. (G) Graphs representing average nucleus angular displacements of t-CTs with different sizes. Each line in each graph represents a t-CT. (H) Graph showing the percentage of CeR events observed in t-CTs of different diameters ( $n = 11$  to 29 for each condition). Scale bars, 50  $\mu\text{m}$ .

projections showed that all cells uniformly moved in the azimuthal direction with small angular deviations in the velocities (movie S5 and fig. S4A), demonstrating a whole-tissue collective rotation. We plotted  $|\vec{V}_\theta|$  for each experiment as a function of diameter and found a nonmonotonic trend with a peak at  $\emptyset = 100 \mu\text{m}$  (Fig. 2C and fig. S4B). In addition, a threshold of  $\emptyset = 150 \mu\text{m}$  was identified, above which no CeR was observed. This threshold may be attributed to the intrinsic dynamics of MDCK epithelial cells whose velocity correlation length was measured to be  $\sim 200 \mu\text{m}$  on flat unconfined surfaces (37, 38). In the range of  $\emptyset = 25$  to  $150 \mu\text{m}$ , we found that CeR duration and azimuthal velocity correlation length,  $\xi_\theta$ , increased with the diameter (see Fig. 2, D and E, and Materials and Methods). The relationship between  $\xi_\theta$  and the diameter was in good agreement with our previous observations in advancing t-CTs (21), corresponding to cellular behaviors constrained by geometry. When analyzing average cell movement over time (for instance,  $V_\theta$  in a 75- $\mu\text{m}$  t-CT; Fig. 2F, left), we found that the emergence of CeR

was correlated to a sudden increase in  $V_\theta$  from nearly zero to about 10  $\mu\text{m}/\text{hour}$  within 2 hours (movie S4). In contrast,  $V_z$  for the same t-CT fluctuated with time without any particular trend (Fig. 2F, right). Spatiotemporal kymograph for  $V_\theta$  showed a clear border marking the CeR starting time point between two distinct velocity patterns (i.e., different color patterns) for nonrotation and rotation regions (Fig. 2G, left). On the contrary, the kymograph for  $V_z$  demonstrated similar patterns before and after that time point (Fig. 2G, right).

Under nonconfluent conditions with advancing t-CTs (21), we also observed synchronized rotations with collective forward helical movement (fig. S5 and movie S6), which lasted longer than those transient rotations within 2D advancing cohorts (37). Among confluent PDMS microtubes, two adjacent groups of cells in a t-CT could occasionally rotate in opposite directions, generating a shear border, and eventually, the whole tissue coordinated and rotated uniformly in one direction ( $n = 7$  of 9; movie S7 and fig. S6A). In

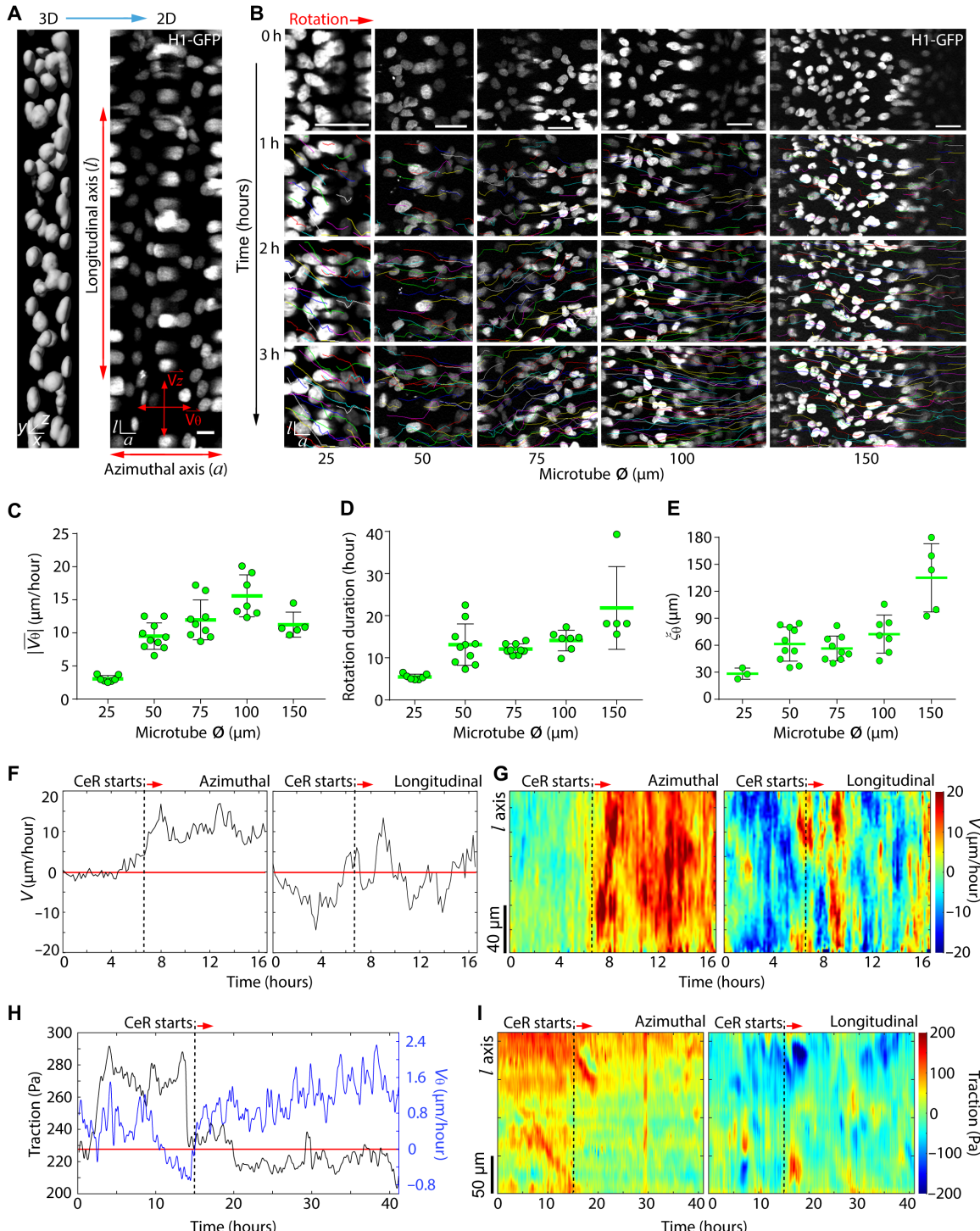


**Fig. 2. Characteristics of epithelial tissue rotation inside microtubes.** (A) Transform of a 3D t-CT into a 2D projection for analysis. The azimuthal and longitudinal velocity vectors are shown in red. Scale bar, 20 μm. (B) Cropped time-lapse 2D projections of rotating H1-GFP MDCK t-CT of different sizes. Tracking individual cell nuclei shows cell trajectories as parallel colored lines. Scale bars, 50 μm. (C to E) Graphs showing absolute average azimuthal velocities ( $|\bar{V}_\theta|$ ) (C), CeR duration (D), and  $\bar{V}_\theta$  correlation length ( $\xi_\theta$ ) (E) in different t-CTs ( $n = 3$  to 10 for each condition). Data are presented as individual values with means  $\pm$  SD. (F and G) Representative graphs (F) and kymographs (G) showing average velocity of a t-CT with  $\varnothing = 75$  μm in azimuthal and longitudinal direction and spatial distribution along  $l$  axis as a function of time. (H) Graph presenting the average traction force (TF) ( $T$ ; black line) applied by a t-CT of  $\varnothing = 75$  μm together with average  $\bar{V}_\theta$  (blue line) evolving with time. (I) Kymographs showing spatial distribution of average traction from (H) exerted azimuthally ( $T_\theta$ ) or longitudinally ( $T_z$ ) along  $l$  axis as a function of time. In (F) to (I), vertical black dash lines and red arrows denote onset of CeR.

this case, the average  $V_0$  exhibited a gradual deviation away from zero with time (fig. S6B, top left). The corresponding kymograph (fig. S6B, bottom left) showed two regions of distinct velocity patterns along the  $l$  axis at the early phase (from 0 to 8 hours; fig. S6B), indicating two cohorts rotating in opposing directions. Afterward, the region of one pattern waned as time passed and the other gradually became dominant over the whole  $l$  axis (from 8 to 16 hours; fig. S6B). Under these conditions, we observed larger fluctuations in average  $V_z$  (fig. S6B, right) than the ones obtained without shear. Overall, these results suggest that cells could coordinate their rotational movement via cell-cell interactions, indicating that cell-cell adhesion in concave  $t$ -CTs could play a role in coordinating whole-tissue CeR.

### Reduced cell traction on substrate during collective tissue rotation

Because cell-substrate interaction evolves during collective epithelial migration (29, 39), we then investigated whether the abrupt shift of  $t$ -CT dynamics from a disordered state to a homogeneous CeR could lead to an apparent change in cell traction on the substrate. To measure traction forces (TFs) of  $t$ -CTs applied on the microtube inner walls, we used soft silicone microtubes ( $52.3 \pm 3.3$  kPa in Young's modulus and  $\varnothing = 75 \mu\text{m}$ ). Because of the fact that CeR is a rotating movement around a long axis without a leading front, to simplify calculation, we sampled a narrow window at the bottom of the microtubes (movie S8), where curvature effects could be neglected. Before CeR started, there were no clear patterns of TFs, and the average traction largely fluctuated with time (from 0 to 15 hours; Fig. 2H). After the onset of CeR, we measured a sheer drop in average TF ( $34.2 \pm 13.2$  Pa;  $n = 5$ ). This reduced traction was then maintained throughout the whole CeR period with reduced fluctuation

(from 15 to 40 hours; Fig. 2H). Such a reduction was mainly attributed to a decrease in TF in the azimuthal direction,  $T_0$ , because  $T_z$  (longitudinally exerted TF) remained relatively stable with time (Fig. 2I). We found a clear change in the  $T_0$  patterns in the kymograph before and after the commencement of CeR, while the  $T_z$  patterns remained unaltered (Fig. 2I). Briefly, our data demonstrated curvature-sensitive CeR dynamics with a threshold of  $\varnothing = 150 \mu\text{m}$  and a sudden decrease in average  $T_0$  after the onset.

### Convex CTs on microfibers show a similar rotational movement

Because substrate curvature is known to regulate collective behaviors and cell-substrate interactions (21, 40–42), we questioned whether a reverse curvature could cause different tissue dynamics. By growing H1-GFP MDCKs outside PDMS fibers of varying diameters (Fig. 3A and fig. S7, A and B), we achieved convex CTs on fiber ( $f$ -CTs) of inverted apicobasal polarity (fig. S7C). Unexpectedly, we also observed similar CeR behaviors in  $f$ -CTs (movie S9 and fig. S7, D and E) as those of  $t$ -CTs in more than 70% of these convexly curved epithelial tissues (fig. S7F). They presented alike CeR duration (Fig. 3B) and a nonmonotonic trend of  $|\bar{V}_0|$  as diameter increased, which peaked at  $\varnothing = 75 \mu\text{m}$  (Fig. 3C). The threshold for CeR to emerge in  $f$ -CTs was  $\varnothing \leq 100 \mu\text{m}$ , whereas  $f$ -CTs of  $\varnothing > 100 \mu\text{m}$  did not rotate ( $n = 6$ ). In addition, MDCK  $f$ -CTs on fibronectin-/Matrigel-/poly-L-lysine-coated (fig. S8) microfibers collectively rotated in a similar fashion. Furthermore, TF microscopy (TFM) on  $f$ -CTs was performed on comparably soft silicone microfibers ( $64.6 \pm 4.0$  kPa in Young's modulus and  $\varnothing = 75 \mu\text{m}$ ). There was also a clear reduction in the profile of average traction after the onset of CeR (Fig. 3D). Furthermore, such a decrease was mainly attributed to a decrease in  $T_0$  (Fig. 3E). In comparison with the case of  $t$ -CTs (a reduction of

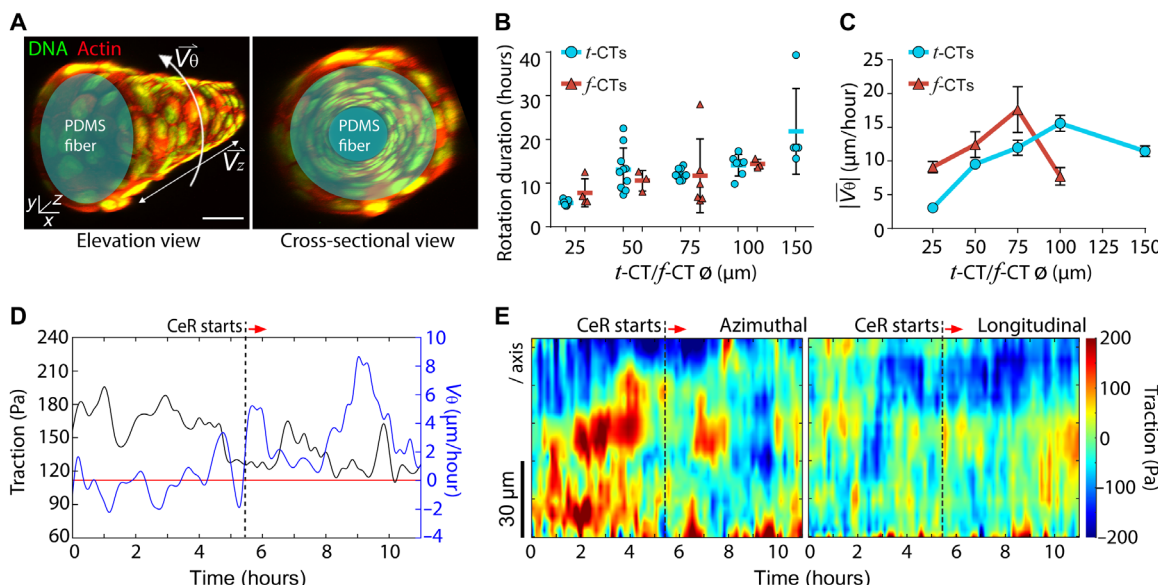


**Fig. 3. Convex CTs show collective cell rotation.** (A) Representative 3D reconstructed images of H1-GFP MDCK cells on  $\varnothing = 100 \mu\text{m}$  PDMS microfiber (marked by teal) showing a convexly curved  $f$ -CT. Actin, red; nuclei, green (H1-GFP). White arrows show either  $\bar{V}_0$  or  $\bar{V}_z$ . Scale bar,  $50 \mu\text{m}$ . (B) Graph displaying CeR duration of different  $t$ -CTs (aqua) and  $f$ -CTs (red). Data are presented as individual values with means  $\pm$  SD. (C) Graph showing  $|\bar{V}_0|$  of different  $t$ -CTs (aqua) and  $f$ -CTs (red). Data are presented as means  $\pm$  SD.  $n = 5$  to 10 ( $t$ -CTs) and  $n = 3$  to 8 ( $f$ -CTs) for each diameter. (D) Graph presenting the average magnitude of traction (black line) applied by an  $f$ -CT on a  $\varnothing = 75 \mu\text{m}$  soft silicone fiber together with average azimuthal velocity (blue line) as a function of time. (E) Kymographs showing time-evolving average  $T_0$  and  $T_z$  from (D) along  $l$  axis. In (D) and (E), vertical black dash lines and red arrows indicate onset of CeR.

$34.2 \pm 13.2$  Pa; Fig. 2H), the magnitude of the decrease was smaller ( $12.1 \pm 11.7$  Pa;  $n = 4$ ). The difference between *f*-CTs and *t*-CTs might originate from different cell-substrate interactions due to different curvatures. Previous investigations have demonstrated that cell scale curvature could affect focal adhesion (FA) organization and dynamics (43), which would profoundly influence pluricellular protrusion orientations (44) and cell polarity (45). In our case, it was possible that *t*-CTs and *f*-CTs responded to distinct curvatures with different tissue organizations and mechanics. The distinct mechanisms then led to different variations in TFs during CeR and deserved future investigations. Besides this difference, we concluded that CeR could emerge in MDCK CTs regardless of the positive or negative tissue curvatures.

### 3D curved epithelial tissues adapt distinct organization of actomyosin networks according to their curvatures

Cellular actin networks are known to respond to substrate curvature (20–22). We then examined whether rotating MDCK CTs of concave and convex curvatures accommodated alike or distinct actin cytoskeleton organizations. We found that basal actin filaments aligned longitudinally inside concave *t*-CTs while azimuthally in convex *f*-CTs (Fig. 4A). Such a sharp contrast in actin filament orientations according to tissue geometries manifested in curved CTs of  $\emptyset \leq 100$   $\mu\text{m}$  in both cases (Fig. 4B). In CTs of larger diameters, actin became isotropic (Fig. 4B), suggesting a synchronized effect of curvature and confinement (21, 22). Notably, using MDCKs expressing myosin-IIA red fluorescent protein (RFP), we found that myosin-IIA networks in rotating *t*-CTs showed the same orientation as actin (fig. S9A and movie S10). Therefore, upon a certain degree of confinement, concavely curved MDCK *t*-CTs adopted longitudinally aligned actomyosin networks that were perpendicular to the direction of their CeR. On the contrary, convexly curved *f*-CTs had the azimuthally aligned actin networks that were oriented along their CeR direction. In addition, the formation of these oriented actin networks was confirmed in MDCKs expressing LifeAct-GFP (fig. S9B) and recurred in both fibronectin-coated (Fig. 4B) and Matrigel-coated (fig. S9C) PDMS microtubes. In the case of *t*-CT, it might not link to substrate rigidity either because basal actin in Matrigel-embedded [ $33.3 \pm 1.6$  Pa in Young's modulus for Matrigel versus  $\sim 1$  to 2 MPa for PDMS (46) microtubes] MDCK ducts also presented *l* axial alignment (fig. S9D). Despite these changes in the nematic alignment of actomyosin cytoskeleton, cell shape within CTs showed no preferential orientation (fig. S9E). In addition, conventional ventral actin SFs that are attached to FAs at the cell edges might form and align in a similar fashion (fig. S10). We further noticed that these actin filaments might extend over multiple cells via CCJs (Fig. 4, A and C), suggesting that they might interact with cell-cell adhesions for mechanical force transduction (47). Briefly, we observed that actin networks oriented in distinct directions according to the curvature of the tissues (see also section S6).

### CCJs of different orientations bear anisotropic tensions

On the basis of the above observations, we then questioned the relationship between CCJs and oriented actin filaments. The former is anchored to and relies on actin networks to withstand substantial forces (48). We found that E-cadherin (E-cad), a key cell adhesion molecule, showed no preferential distribution in variously oriented CCJs in both MDCK wild-type (WT) *t*-CTs and *f*-CTs (fig. S11). In contrast, another component of adherens junctions,  $\beta$ -catenin (49),

formed finger-like structures in parallel to the basal actin alignment, i.e., aligning in longitudinal or azimuthal directions for *t*-CTs or *f*-CTs (Fig. 4C), respectively. As a result,  $\beta$ -catenin was preferentially recruited to the CCJs that were perpendicular to the basal actin networks in either case (Fig. 4D).  $\beta$ -Catenin is known to link to actin cytoskeleton via  $\alpha$ -catenin, a key receptor for transmembrane cadherin adhesion complexes (50). Looking at the marker ( $\alpha$ -18) for tension-bearing  $\alpha$ -catenin (51), we also found an anisotropic distribution of unfolded (i.e., bearing tensions)  $\alpha$ -catenin to CCJs, where the  $\beta$ -catenin fingers were seen (Fig. 4D). These findings suggested that the CCJs in *t*-CTs that were parallel to CeR direction ( $V_\theta$  direction; Fig. 4D, left, violet  $\alpha$ -18 enriched CCJ) were bearing tensions, as opposed to *f*-CTs, where tension was supported by CCJs perpendicular to  $V_\theta$  (Fig. 4D, right, violet  $\alpha$ -18 enriched CCJ). These findings showed that large coordinated collective movements could emerge despite different molecular organizations of cytoskeleton and CCJ. These organizations are known to promote tension anisotropy, as previously described in other systems (52, 53), and accommodate geometric constraints. This was supported by our findings that *t*-CTs continued rotating even when tissue contractility was mitigated by a Rho-associated protein kinase (ROCK) inhibitor, Y-27 (movie S11) (54). Disrupting CCJs using EGTA eliminated aligned actin filament organizations (Fig. 4, E and F). The profound interdependence of CCJs and actin alignment and the emergence of anisotropic tension and various planar polarities in curved epithelial tissues deserve further investigation.

### Proper cell-cell adhesions are essential for CeR

CCJs are known to play an important role in collective cell migrations in various in vivo and in vitro systems (55). In our attempts using EGTA to disrupt CCJs, we found that this treatment halted CeR, while CeR recurred in both concave and convex CTs after EGTA washout (Fig. 5, A and B). This is different from 2D epithelial rotation in rings (10), which remains unaffected upon EGTA treatment. We then inactivated the E-cad gene using CRISPR-Cas9 (38). E-cad knockout (KO) in MDCKs weakened the cell-cell adhesions, but cells could still maintain their contact through another cadherin (cadherin-6; fig. S12) (38). We observed similar CeR in both E-cad KO *t*-CTs and *f*-CTs (fig. S13 and movie S12). Nevertheless, E-cad KO resulted in a substantially shorter velocity correlation length ( $\xi = \sim 140$   $\mu\text{m}$ ) in comparison with MDCK WT ( $\xi = \sim 200$   $\mu\text{m}$ ) (38). This led to a decrease in the CeR thresholds [ $\emptyset \leq 100$   $\mu\text{m}$  for E-cad KO *t*-CTs ( $n = 11$ ) and  $\emptyset \leq 50$   $\mu\text{m}$  for E-cad KO *f*-CTs ( $n = 22$ )]. In addition, E-cad KO caused marked reductions in CeR event percentages (fig. S13A) and rotation speeds (fig. S13, B, C and E), although cells could maintain coordinated rotation for hours (fig. S13, C to F).

To further perturb CCJs, we simultaneously knocked out E-cad and cadherin-6 in MDCK cells (MDCK cadherin double KO). These MDCK cadherin double KO cells lost  $\beta$ -catenin expression at the adherens junctions (fig. S12) and did not show CeR in either *t*-CTs ( $n = 15$ ) or *f*-CTs ( $n = 15$ ) in the range of  $\emptyset = 50$  to 100  $\mu\text{m}$  even at their confluence (fig. S14 and movie S13). In addition, we formed *t*-CTs ( $n = 16$ ) or *f*-CTs ( $n = 8$ ) using MDCK  $\alpha$ -catenin knockdown ( $\alpha$ -cat KD) cells (37) on both concavely and convexly curved scaffolds. Similarly, these cells showed alike features of random motions in  $V_\theta$  and  $V_z$ , as well as their corresponding kymographs (fig. S15). Together, these results showed that the establishment and maintenance of collective cell rotation required stable cadherin-mediated CCJs in response to cylindrical curvatures.

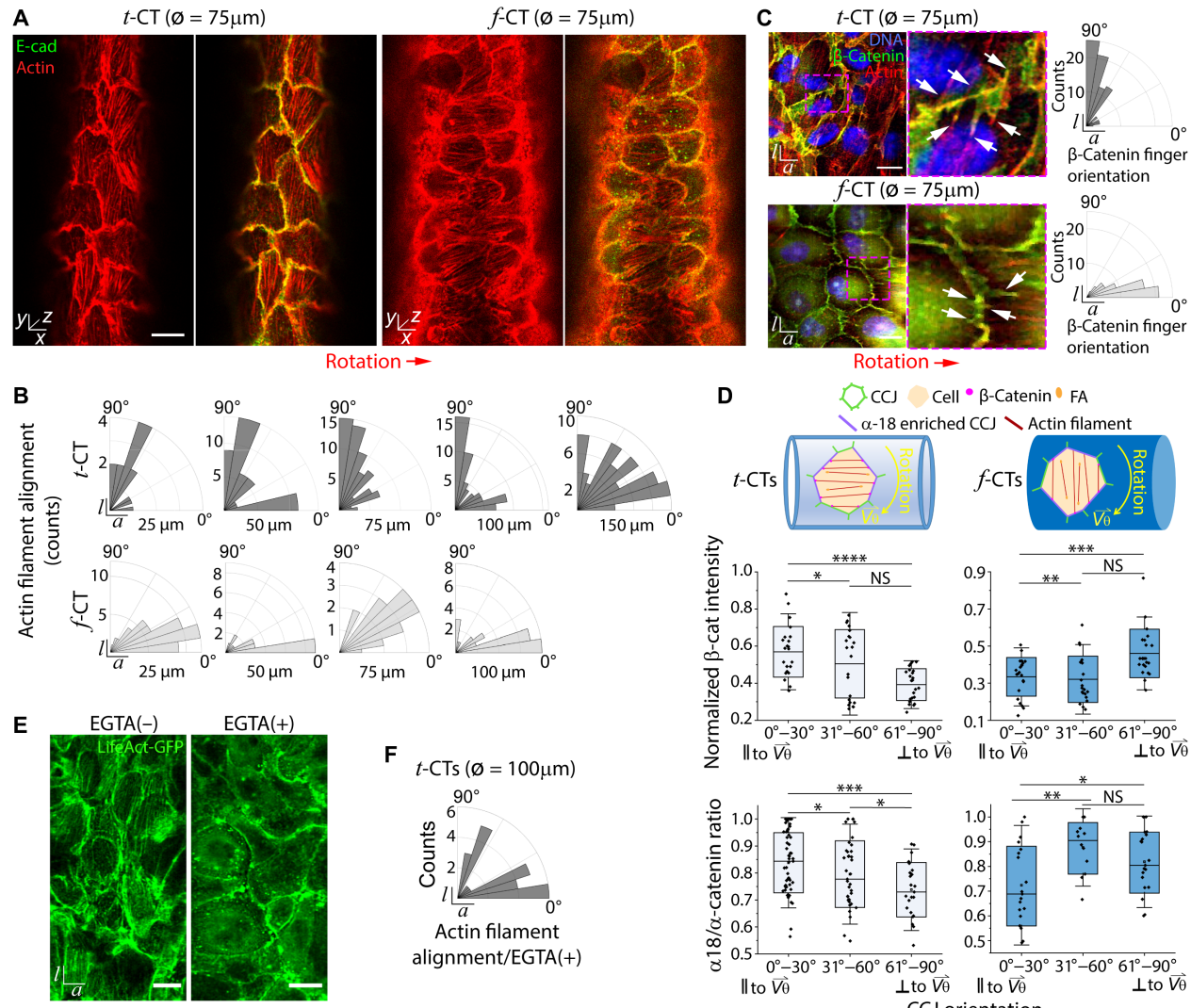


**Fig. 4. Different organizations of actin cytoskeleton and CCJ according to tissue curvatures.** (A) Representative 3D reconstructed images of rotating MDCK *t*-CTs and *f*-CTs showing large-scale long-range basal actin filaments orienting in different directions. Actin, red; E-cadherin (E-cad), green. (B) Rose diagrams of actin filament orientation in CTs of varying diameters ( $n = 13$  to 75). (C) 2D projections of a *t*-CT (top) and a *f*-CT (bottom) showing detailed features of CCJs in different orientations. White arrows indicate actin filaments overlapping with  $\beta$ -catenin fingers. Magenta dashed boxes indicate zoomed-in regions. Rose diagrams on the right showing the orientation of  $\beta$ -catenin fingers at CCJs ( $n = 88$  for *t*-CTs and  $n = 65$  for *f*-CTs) with respect to the azimuthal axis. (D) Top: Schematic representation of actin alignment and distribution of  $\beta$ -catenin and  $\alpha$ -18 enriched CCJs in *t*-CTs and *f*-CTs. Actin filaments may attach to CCJs via  $\beta$ -catenin and substrate via FA. Middle and bottom: Normalized  $\beta$ -catenin fluorescent intensity (middle;  $n = 68$  for *t*-CTs and  $n = 65$  for *f*-CTs) and fluorescent intensity ratio of unfolded  $\alpha$ -catenin ( $\alpha$ -18) over total  $\alpha$ -catenin (bottom;  $n = 115$  for *t*-CTs and  $n = 50$  for *f*-CTs) in various oriented CCJs. The relative angles between CCJs and CeR direction (i.e., relative to  $\alpha$  axis) were presented in x axis. Data are shown as individual values overlapped with box charts showing means  $\pm$  SD (coefficient = 1 for the box and coefficient = 1.5 for the whiskers). NS, not significant. (E) 2D fluorescent projections showing organization of actin (LifeAct-GFP) in a *t*-CT with  $\phi = 100\mu\text{m}$  before and after EGTA treatment ( $n = 26$ ). \* $P < 0.05$ , \*\* $P < 0.01$ , \*\*\* $P < 0.001$ , \*\*\*\* $P < 0.0001$ .

Downloaded from https://www.science.org on April 09, 2025

### Roles of lamellipodial protrusions in CeR

After investigating the roles of CCJ stability, we asked how protrusive forces usually generated by actin filaments could affect CeR. Using high-resolution time-lapse imaging, we found that the long-range, basal actin filaments in both *t*-CTs and *f*-CTs remained persistently immobile related to the substratum during CeR (Fig. 5C and movie S14) and may disappear when they reached the rear edge of the cell. In addition, we found that actin-based cryptic lamellipodia continuously appeared at the cell edges (Fig. 5D). These protrusions were highly aligned with the CeR direction, regardless of the oriented actomyosin

networks (Fig. 4, A and B, and fig. S9, A and B) and the random cell orientation (fig. S9E) in all confluent CTs. To check whether these were polarized structures, we monitored yellow fluorescent protein-p21 binding domain (YFP-PBD) signals as a marker for active Rac-1 and Cdc42 and found that cells accumulate Rac-1 at their fronts as they protruded forward (fig. S16), suggesting the role of polarized protrusions in CeR. This was supported by treatment with a Rac-1 inhibitor (Z62), which immediately halted CeR (Fig. 5E). Overall, we identified immobile long-range actin filaments in rotating *t*-CTs and *f*-CTs while polarized cellular protrusions as essential factors for persistent CeR.

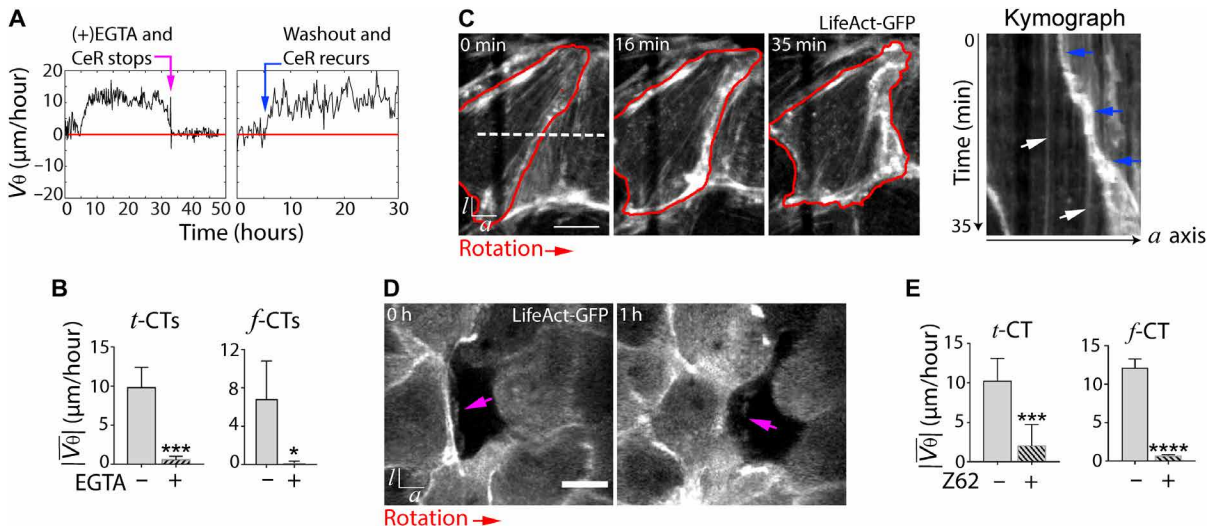


**Fig. 5. Roles of cell-cell adhesions and cell polarity in rotating CTs.** (A) Graphs showing EGTA treatment ceased CeR ( $V_\theta \approx 0$ ; magenta arrow) and CeR recurrence (blue arrow) after washout. (B) Plots presenting  $|V_\theta|$  for different rotating CTs before and after EGTA treatment ( $n=4$  for all cases). (C) 2D time-lapse (15 s per frame) projections demonstrating actin dynamics of a  $t$ -CT ( $\emptyset = 100 \mu\text{m}$ ) expressing LifeAct-GFP during CeR. The cell periphery is drawn in red. The kymograph on the right was obtained by reslicing along white dashed line (0 min). White arrows indicate trajectories of immobile long-range actin filaments, and blue arrows show displacement of cell front with respect to  $a$  axis. (D) 2D time-lapse projections demonstrating actin-based cryptic protrusion of a rotating  $t$ -CT ( $\emptyset = 100 \mu\text{m}$ ) consisting of WT and LifeAct-GFP MDCKs. Magenta arrows denote lamellipodial protrusions of a LifeAct-GFP-expressing cell toward a WT (unmarked) cell. (E) Graphs presenting  $|V_\theta|$  for different rotating CTs before and after Z62 treatment ( $n=6$  for  $t$ -CTs and  $n=3$  for  $f$ -CTs). Student's  $t$  test,  $*P < 0.05$ ,  $***P < 0.001$ , and  $****P < 0.0001$ . In (B) and (E), data are presented as means  $\pm$  SD. Red arrows indicate rotation direction. Scale bars, 20  $\mu\text{m}$ .

### An active polar gel description for CeR

To gain insights into 3D CeR, we used an overdamped active polar fluid framework (56–58) including explicit couplings between substrate curvature and cell polarity (see sections S1 and S2). To describe MDCK CTs, we accounted for an average cell polarity and an average cell velocity given by a polarity field  $\mathbf{p}$  and a velocity field  $\mathbf{v}$ , respectively. Here, the polarity field  $\mathbf{p}$  can represent an averaged direction of planar polarity in cell monolayers, such as cryptic lamellipodia on one side of cells. In cylindrical geometries, the principal directions of a cylindrical substrate are the longitudinal direction  $\hat{z}$  and the azimuthal direction  $\hat{\theta}$  ( $l$  and  $a$  in the experimental section, respectively; Fig. 6A). In addition, the substrate curvature along the longitudinal direction vanishes, and along the azimuthal direction is  $1/R$ , where  $R = \emptyset/2$  is the substrate radius. The curvature  $1/R$  changes sign when describing concave (negative) or convex (positive) curvatures corresponding to microtubes and microfibers, respectively. In this case, we allowed  $R$  to change sign to account for different curvatures, i.e.,  $R < 0$  for microtubes and  $R > 0$  for microfibers.

To describe the effects of substrate curvature on cell polarity, we accounted for couplings allowed by symmetries between the substrate curvature and the polarity field. For cylindrical substrates, we found that the equilibrium uniform polarity states are determined as the minimum of an effective free-energy density  $f$  (see sections S1 to S3 for a derivation of  $f$  as a thin-film limit of a 3D Landau-Ginzburg free-energy density)

$$f = \left( \chi_2 + \frac{\bar{\beta}_1}{R} + \frac{\bar{\beta}_2}{R^2} \right) \frac{(p_z^2 + p_\theta^2)}{2} + \left( \frac{\beta_1}{R} + \frac{\beta_2}{R^2} \right) \frac{p_\theta^2}{2} + \chi_4 \frac{(p_z^2 + p_\theta^2)^2}{4} \quad (1)$$

where  $p_z$  and  $p_\theta$  are the components of the polarity field  $\mathbf{p}$  in the longitudinal and azimuthal directions, respectively. In view of the

fact that confluent MDCK cell monolayers are, on average, immobile on a flat substrate (59, 60), we considered that a disordered state dominates for a sufficiently large radius  $R$  and set the phenomenological parameters  $\chi_2 > 0$  and  $\chi_4 > 0$ . For intermediate  $R$ , the substrate curvature can induce ordered states via couplings with the polarity field. The parameters  $(\beta_1, \bar{\beta}_1)$  and  $(\beta_2, \bar{\beta}_2)$  are amplitudes associated with linear and quadratic couplings in  $1/R$  and the polarity field, respectively. Hence, the linear couplings  $(\beta_1, \bar{\beta}_1)$  change sign with curvature [i.e., convex (positive) to concave (negative)], whereas the quadratic couplings  $(\beta_2, \bar{\beta}_2)$  do not (Fig. 6A). As a result, quadratic couplings may lead to collective rotation in both concave and convex CTs, while linear couplings may only cause CeR under either one of the conditions.

The radius  $R$  then determines the state of CTs (either rotation or no rotation; see sections S3 and S4 for details). Within the parameter regime where  $\bar{\beta}_1 = \bar{\beta}_2 = 0$  in Eq. 1, the system can either assume a disordered phase (no rotation), whereby  $p_z = p_\theta = 0$ , or an azimuthal ordered phase (rotation), whereby  $p_z = 0$  and  $p_\theta = \pm \mathcal{P}$  (Fig. 6B and sections S3 and S4), where  $\mathcal{P}$  depends on  $R$  and material parameters. In the overdamped limit, force balance in the azimuthal direction leads to the steady-state azimuthal velocity field in the azimuthal ordered phase (see section S4)

$$v_\theta = \pm \frac{T_0 \sqrt{\chi_2/\chi_4}}{\xi(1 + \alpha_2/r^2)} \sqrt{-\left(1 + \frac{1}{r} + \frac{\alpha_1}{r^2}\right)} \quad (2)$$

which depends only on two dimensionless parameters  $\alpha_1 = \beta_2 \chi_2 / \beta_1^2$  and  $\alpha_2 = \eta \chi_2^2 / \xi \beta_1^2$  and the dimensionless radius  $r = R \chi_2 / \beta_1$ . The parameter  $\eta$  corresponds to the shear viscosity,  $\xi$  corresponds to a friction coefficient with the underlying substrate, and  $T_0$  corresponds to the amplitude of polar traction forces. With this, we found that the direction of  $p_\theta$  and  $v_\theta$  is set by a symmetry-breaking process without sign

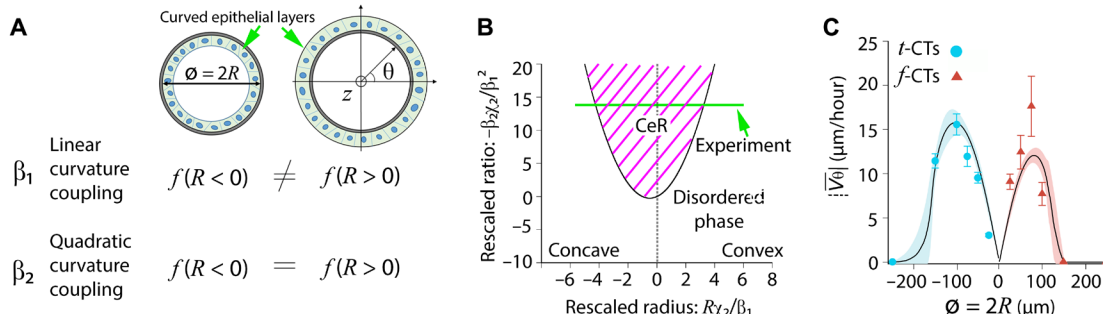


**Fig. 6. An active polar gel description for 3D collective tissue rotation and polarization.** (A) Schematic representation of cross-sectional views of a cell monolayer that lays on either the inner (left; i.e., t-CT) or the outer (right; i.e., f-CT) side of a cylindrical substrate (dark gray). Couplings linear to the curvature ( $\beta_1$ ) distinguish between both configurations, whereas couplings quadratic to the curvature ( $\beta_2$ ) do not. The free-energy density  $f$  is given by Eq. 1. We use the convention that  $R < 0$  for microtubes (t-CT) and  $R > 0$  for microfibers (f-CT). In this framework,  $z$  and  $\theta$  denote the longitudinal direction and the azimuthal direction of the cylindrical substrate. (B) Phase diagram of steady-state uniform solutions as a function of the rescaled substrate radius  $R\chi_2/\beta_1$  and the effective parameter  $-\beta_2\chi_2/\beta_1^2$ . The two solutions (separated by the black parabola) correspond to a disordered phase and a collective rotating phase (indicated by magenta slashed shaded area). In our experiments, we sample the  $x$  axis of the phase diagram by varying the radius of microtubes/microfibers,  $R$ . The parameter region that fits best the experimental velocity curves from (C) is indicated by the green line parallel to the  $x$  axis. To sample the  $y$  axis, one can alter intrinsic epithelial properties, such as enhancing/weakening cell-cell adhesions and cell-substrate adhesion. (C) Graph showing azimuthal velocity as a function of CT's diameter. The circular aqua and triangular red dots correspond to the experimental measurements of the azimuthal velocity from (Fig. 3C). The dark curves and shaded aqua/red areas represent the means  $\pm$  SD of the azimuthal velocity given by Eq. 2 for the subset of parameters that satisfies  $\mathcal{E} < 1.1\mathcal{E}_m$ , being  $\mathcal{E}$  as the error function given by eq. S29 in section S5 and  $\mathcal{E}_m$  as the absolute minimum. Parameters  $\bar{\beta}_1 = \bar{\beta}_2 = 0$ .

preference, i.e., no chirality in CeR, in agreement with our experiments in Fig. 1F and fig. S7E. Besides, we found that, in the presence of a free edge, the velocity field is helicoidal and involves a superposition of the azimuthal velocity (Eq. 2) and the longitudinal velocity, which is also in agreement with our findings in fig. S5.

Next, we infer the contribution of linear and quadratic couplings to curvature in CTs by applying our continuum approach to the velocity patterns of CTs in their steady rotational state in a range of  $\mathcal{O}$  from 25 to 250  $\mu\text{m}$  (Fig. 6C and see the fitting procedure in section S5). Our fitting disclosed a region of the parameter space that is compatible with the experimental measurements (Fig. 6C and table S1 in section S5). In this region, the ratio  $|\beta_2/\beta_1| > 200 \mu\text{m}$  is larger than the CeR thresholds ( $\mathcal{O} > 150 \mu\text{m}$  for t-CTs and  $\mathcal{O} > 100 \mu\text{m}$  for f-CTs), showing that quadratic couplings are predominant for CeR in curved CTs. Hence, we concluded that a quadratic coupling of the polarity field in the MDCK CTs to the curvature led to the persistent CeR. Furthermore, using the parameters that fitted our measurements best (Fig. 6C), we identified an experimental trajectory by changing  $R$ , which traversed both the CeR and disordered phases (Fig. 6B, green line). In this regime, for sufficiently small radius, the azimuthal velocity, set by balancing active TFs and viscous stresses, increases with the substrate radius. For sufficiently large radius, the reduction of the curvature field leads to a reduction of both the polar order parameter and the azimuthal velocity, vanishing above a critical radius (Fig. 6C). This is in agreement with the experimental data that describe the curvature-velocity relationship (Fig. 3C).

Moreover, we studied how the orientation of actin fibrils couples to curvature in MDCK CTs. To describe the average orientation of actin fibrils, we used a director field  $\hat{n}$ . Besides, we consider that actin fibrils exhibit a nematic order, i.e., our theoretical description is invariant under inversions  $\hat{n} \rightarrow -\hat{n}$  and  $|\hat{n}| = 1$ . Then, the previous theoretical approach was extended by including couplings between the director field  $\hat{n}$ , the polarity field  $p$ , and the substrate curvature. We found that the equilibrium uniform states are determined as the minimum of an effective free-energy density that generalizes Eq. 1 (see section S6). To infer the nature of the curvature

couplings that determined actin network organization in MDCK CTs, we compared the equilibrium uniform orientation patterns of  $\hat{n}$  to the experimental case. In our experiments, the orientation of actin fibrils was found, on average, in the longitudinal direction for t-CTs (concave) and in the azimuthal direction for f-CTs (convex) in a range of  $\mathcal{O} = 25$  to 100  $\mu\text{m}$  (Fig. 4, A and B). This observation indicates that linear couplings between the curvature and the director field  $\hat{n}$  are predominant for the organization of actin networks because they change sign with curvature [i.e., concave (negative) to convex (positive)]. This analysis suggests that these linear curvature couplings could arise from different microscopic mechanisms, such as direct interactions between the substrate curvature and the actin fibrils or indirect interactions mediated by cell polarity markers such as cryptic lamellipodia (see section S6).

## DISCUSSION

3D tissue rotation is an interesting phenomenon where a cohort of cells without a free front lines a quadric surface and collectively rotates around an axis. However, even when CeR happens in tissues of explicit curvatures, the relationship between CeR and tissue geometries remains largely unexplored. Using *in vitro* 3D tissue rotational models, we expand the repertoire of CeR beyond current negatively curved epithelial models. We highlight the robustness of CeR on both concavely and convexly curved substrates regardless of apicobasal polarity and cytoskeleton networks. Our experimental findings are well captured by a theoretical approach based on active polar fluid (Fig. 6), where cell polarity, velocity, and actin filaments are coupled quadratically or linearly to the tissue curvatures. Our findings have important implications for our understanding of *in vitro* and *in vivo* tissue behaviors under complex geometrical conditions, concerning front-rear cell polarity, collective cell migration, and long-range actomyosin order.

First, it is intriguing to find that CTs with completely different oriented actin networks demonstrate much alike collective rotational migration. This could indicate that mechanical stresses are

transmitted in different directions in *t*-CTs and *f*-CTs, leading to anisotropic tension in tissues. Given the fact that actin filaments link to both CCJs and FAs, complex cross-talk between cell-cell and cell-substrate may determine the distribution of different actin filaments and tension in the curved tissues. The negative curvature may favor the formation of CCJ-associated actin filaments, while the convex geometry could promote the growth of conventional ventral actin SFs with both ends attached to FAs. The comparison of our active polar gel description to experiments on MDCK CTs suggests that the organization of actin filaments could be explained by two different linear curvature couplings. To further identify the nature of the mechanism, one could study the cross-correlations between the orientation of actin filaments and cell migration on substrates with more complex curvature patterns, such as undulated stripes, or examine their spatiotemporal fluctuations in *t*-CTs and *f*-CTs for a fixed diameter. Nevertheless, CeR emerges regardless of the different actin networks and potentially distinct anisotropic tissue tension distributions. Thus, an intuitive implication could be that CeR is a state-minimizing shear in epithelia whose migratory direction does not necessarily align with principal stress direction in tissue as 2D collective migration (29). Such a mismatch between collective movement and the principal stress direction has been reported in human mammary gland organoids. In these situations, rigid body rotation of nascent alveoli occurs before circumferential tension in the tissue overrides axial one and cell repolarization in the azimuthal direction (6). In our case, helical migration due to the combination of CeR and longitudinal expansion emerges in both nonconfluent *t*-CTs and *f*-CTs, where there is a clear *l*-axial stress. In addition, reduction of mechanical stress in CTs by Y-27 treatment does not block CeR. These findings are in line with the notion that CeR could emerge regardless of different actomyosin and CCJ organizations that promote tension anisotropy.

Nevertheless, the underlying principles and factors that trigger collective polarity for CeR remain unclear. Cellular protrusions seem to be important, and cells tend to protrude on substrates where they could well attach. Whereas in our TFM measurement on *t*-CTs, we find an abrupt decrease in traction  $T_\theta$ . Such an observation reveals a transition in cell-substrate interactions from a chaotic status without defined collective movement to CeR. This may suggest that maintaining CeR does not require strong cell-substrate interactions. Before the CeR onset, cells in the tissue might be grouped into separate clusters that constantly interact with their neighboring cells. This allows long-range force transmission via cytoskeleton and cell-cell adhesions across the entire clusters (16, 39). The kymographs of  $T_\theta$  and  $T_z$  before CeR (Fig. 2I) then demonstrate regional traction distributions. These regional resultant forces could be either positive or negative, and thus, the measurement of the average  $T$  (0 to 15 hours; Fig. 2H) shows large fluctuations with time. Once CeR emerges as a state that may minimize shear (29),  $T_\theta$  mitigates throughout the entire *t*-CT with unchanged  $T_z$ , resulting in a reduced  $T$  (15 to 40 hours; Fig. 2H). This finding may be explained by a possible redistribution of forces from cell-substrate toward cell-cell contacts to promote coordinated motion. Notably, although similar, the decrease in  $T_\theta$  value is less substantial in rotating *f*-CTs. We speculate that the reduction in cell-substrate traction at the onset of CeR could lead to a competition between the active contractility and the bending elasticity of the azimuthally aligned actin filaments (20) in *f*-CTs. The bent actin filaments may still require strong cell-substrate adhesion even after the CeR onset.

This scenario does not exist in *t*-CTs, where the longitudinally aligned actin filaments are not bent. Thus, actin bending in *f*-CTs may require strong and stable cell-substrate interactions. Together, these results indicate that different and indirect roles of varying actomyosin networks in CeRs could exist and how these networks are established and maintained deserve further investigation.

A recent study reveals the existence of immobile actin SFs in *Drosophila* and their role in promoting parallel cell trajectories during collective rotational migration (18). The authors propose a treadmilling behavior that enables SFs to persist in a moving epithelium. This model may resemble the CeR in positively curved *f*-CTs, but we notice that the follicular epithelium in *Drosophila* egg chamber is negatively bent and has an inverted apicobasal polarity. The stationary, azimuthally aligned actin filaments in *f*-CTs may undergo treadmilling by adding new adhesions and actomyosin segments at their fronts. However, our paxillin staining did not reveal multiple adhesions along the actin filaments (fig. S10), and our results show that they could connect to adherens junctions. Furthermore, in *t*-CTs where the actin filaments are aligned perpendicular to CeR direction, cells' trajectories were also mostly in parallel (Fig. 2B). Thus, our results suggest that, at least in MDCK epithelia, cells could keep their parallel trajectories without the support of aligned actin networks while the role of SFs could not be entirely ruled out. As the immobile actin filaments in *t*-CTs have to be disassembled and give space to an incoming cell, it is impossible for these *l*-axial filaments to undergo front-rear treadmilling. Instead, they may slide along the CCJs over time, a phenomenon that is recently found in apical SFs in developing epithelial tissues (61). It is then of high interest to carefully investigate the lifetimes and the nucleation and disassembly mechanisms of both *l*- and *a*-axial actin in the follow-up studies. A scrutinization of the evolution of CCJs and their connections with these oriented actomyosin networks could also provide important information about epithelial organization during CeR. In this work, partial perturbation of CCJs by E-cad KO does not fully block CeR in small CTs but results in notable reductions in CeR event percentages and  $|\nabla\theta|$ . This could be attributed to a substantial decrease in velocity correlation length. Such a change in epithelial properties may correspond to a downwards shifting of the experimental trajectory (green line) on the  $y$  axis in the phase diagram of Fig. 6B, i.e., to regions where the CeR thresholds are smaller. Further perturbation of CCJs (MDCK cadherin double KO and  $\alpha$ -cat KD) leads to the blockage of CeR in all situations and random motions in  $V_\theta$  and  $V_z$  even at a high confluence, highlighting the essential role of CCJ stability in CeR.

Our combined experimental and theoretical approach proposes a framework to understand the emergence of collective cell dynamics on cylindrical curvatures. Together, this work presents a reductionist experimental approach and biophysical modeling to explore CeR in both concavely and convexly curved epithelia. The reverse organization between actin structures and junctional complexes in microtubes and on microfibers demonstrates that molecular functional components can adapt to geometrical constraints to favor similar behaviors at the multicellular level. We anticipate that these versatile functional structures may help cells to navigate their environment. Our model enables future investigations into rotating tissues of different actomyosin networks, apicobasal polarity, and actin-CCJ interactions, thus offering opportunities to shed light on the functional link between tissue mechanics and tissue development.

## MATERIALS AND METHODS

All experiments were conducted according to the regulations of the French legislation and European Union guidelines. Approval by an ethics committee is not required for experiments using MDCK cell lines.

### Live imaging on zebrafish embryos

Zebrafish Tg(cldnb:lynEGFP) transgenic lines (gift from D. Gilmour) (62) were raised at 28°C and kept under standard laboratory conditions according to European Union guidelines for the handling of laboratory animals. The use of zebrafish was approved by the Comité d’Ethique pour l’Expérimentation Animale and the Direction Sanitaire et Vétérinaire de l’Hérault (CRBM aquatic facility, C-34-172-39). Embryos were staged according to hours post-fertilization. One-cell-stage embryos were injected with 100 pg of H2B-mCherry mRNA. Capped mRNAs were synthesized with the mMessage mMachine SP6 in vitro transcription kit (Ambion, Thermo Fisher Scientific) using PCS2 + H2B-mCherry (gift from P. Keller; Addgene, plasmid #99265; [www.addgene.org/99265/](http://www.addgene.org/99265/)) as template. Before live imaging, 24-hpf zebrafish embryos were manually sorted on the basis of their fluorescence and dechorionated. 1-Phenyl-2-thiourea (Sigma-Aldrich) was then used to remove pigmentation according to standard protocols. For live imaging, embryos are anesthetized with tricaine methanesulfonate (0.2 mg/ml; Sigma-Aldrich, MS222) until larvae are motionless and nonresponsive to a touch stimulus. Embryos were then mounted in 1% low-melting agarose containing in E3 medium on eight-well microscopy slides (Ibidi). Additional tricaine/E3 is added to fill the culture dish. Time-lapse imaging of the pronephros was acquired using a spinning disk microscope driven by Fusion software: Inverted Nikon microscope coupled to a Dragonfly Andor spinning disk, EMCCD iXon888 Life Andor, 40× Apo/1.15 numerical aperture/working distance of 0.6 mm per water. Images were recorded every 5 min (*z* stack of 1 μm interval) between 34 and 51 hpf. Image processing (cropping, rotation, drift correction, brightness, and contrast adjustment) were performed with Fiji or Imaris (Bitplane) software.

### MDCK cell culture

MDCK WT cells, MDCK-H1-GFP (stable cell line transfected with H1-GFP), MDCK-LifeAct-GFP (stable cell line transfected with LifeAct GFP, binding to actin filaments), MDCK-PBD-YFP (stable cell line expressing the YFP-PBD probe of activated Rac1 and Cdc42; provided by F. Martin-Belmonte, Universidad Autónoma de Madrid), MDCK-myosin-II-RFP (stable cell line transfected with myosin-II RFP), MDCK E-cad KO, MDCK double cadherin KO, and MDCK α-cat KD were cultured in complete Dulbecco’s modified Eagle’s medium (DMEM) (Life Technologies), supplemented with 10% fetal bovine serum and 1% penicillin/streptomycin. All cells were cultured at 37°C under 5% CO<sub>2</sub> conditions.

### Generation of MDCK cadherin double KO cell line

MDCK E-cad (encoded by *CDH1*) and cadherin-6 (encoded by *CDH6*) double KO stable cells were generated from MDCK E-cad KO (38) using a pair of CRISPR-Cas9 plasmids (Addgene, 48138 and 62988). The two following guide RNA sequences were used: CACCGGGATATACTAGGCCACCAAG and CACCGGTTGTG-TATAGTATCCTACA. Around 5 million cells were electroporated (Neon Transfection System Invitrogen) with 10 μg of plasmid in one pulse of 20 ms and at 1650 V. Twenty-four hours later, cells

were selected by adding puromycin (2 μg/ml) in the culture medium. Twenty-four hours later, GFP-positive single cells were sorted in 96-well plates by flow cytometry using an Influx 500 sorter analyzer (BD Biosciences). The clonal populations were then selected on the basis of the absence of β-catenin by immunofluorescence staining. The absence of cadherin-6 in the clones generated was confirmed by Western blot analysis of protein extracts (fig. S13).

### Western blot

Proteins for MDCK cells were extracted using lysis buffer [100 mM tris (pH 7.5) + 150 mM NaCl + 0.5% NP-40 + 10% glycerol + 0.5% Triton X-100] containing 1× protease inhibitor cocktail (Roche) and 1× phosphatase inhibitor (PhosphosSTOP, Roche). Protein (20 μg) was loaded onto NuPAGE 4 to 12% bis-tris gel using a mini gel tank and dry-transferred using an iBlot transfer system (Invitrogen). Nonspecific sites were blocked using 5% nonfat dry milk in 0.1% phosphate-buffered saline (PBS) with Tween 20. Primary antibodies (glyceraldehyde-3-phosphate dehydrogenase from Thermo Fisher Scientific, reference mA5-15738, or cadherin-6 from Cell Signaling Technology, reference 48111) were diluted in PBS with Tween 20 at 1:1000, and the blots were incubated overnight on a shaker at 4°C. The blots were then washed three to four times for 10 min each in PBS with 0.1% Tween 20 and incubated with either horseradish peroxidase-linked (Pierce) or Dylight 800 (Thermo Fisher Scientific)-linked secondary antibodies at 1:10,000 for 2 hours. The blots were then washed three times PBS with 0.1% Tween 20 or tris-buffered saline with Tween 20 for 10 min each. The blots were then revealed using ChemiDoc MP (Bio-Rad) using SuperSignal West Femto (Thermo Fisher Scientific, 34095) or chemiluminescence.

### Culture of Matrigel-embedded MDCK cysts and ducts

To culture MDCK cysts and ducts within Matrigel (Corning, #734-1100), we adopted and adjusted methods described previously (31, 63). Briefly, detached MDCK H1-GFP cells (10<sup>4</sup> cells/ml) were suspended with 50% Matrigel (diluted in complete DMEM) by repetitive pipetting. Drops (100 μl) of cell-Matrigel mixture were transferred to a precooled glass-bottom petri dish (FluoroDish, catalog no. FD35-100) and incubated at 37°C for 1 hour for gel polymerization. The cell-Matrigel drops were then overlaid with 3 ml of complete DMEM for long-term culture. The medium was changed every 2 days. Typically, MDCK cysts and ducts developed after culturing for 6 days, and fluorescent microscopy imaging was performed between 7 and 10 days after cell seeding.

### Microfabrication of elastomeric microtubes and microfibers

Microtubes were fabricated inside PDMS blocks as described previously (21). Briefly, smooth copper or platinum wires (Goodfellow SARL) of different diameters were aligned in parallel 1 to 2 μm above a silicon wafer (1 cm by 1 cm) using a precise stage (64) that could control the positions of each wire. A fresh mixture of silicone elastomer base and silicone elastomer curing agent (Sylgard 184, DOWSIL; 10:1, w/w) was poured on the silicon wafer to cover the metal wires. The entire setup was then left at room temperature for 24 hours for PDMS polymerization. After the polymerization, the metal wire was pulled out during a sonication process in an acetone solution, forming parallel microtubes in a PDMS block. As-fabricated PDMS blocks were then heated up to 80°C in an oven for 30 min to remove any acetone remnant. The PDMS blocks containing straight, parallel microtubes were later cut in a direction perpendicular to

the microtubes into small pieces of ~0.5 to 1 mm (this is also the length of the microtubes) in the width. These small pieces were then stuck to a glass-bottom petri dish (FluoroDish, catalog no. FD35-100) for protein functionalization. The two openings of the microtubes allowed efficient diffusion of medium throughout, avoiding creation of a biochemical gradient inside the microtubes.

To fabricate PDMS microfibers, freshly mixed silicone elastomer base and curing agent (Sylgard 184, DOWSIL; 10:1, w/w) were left at room temperature for about 10 hours to allow viscosity of the mixture to increase. PDMS microfibers of different sizes were then pulled out of the viscous mixture at different speeds using 200- $\mu$ l pipette tips. As-fabricated microfibers were hanged in an 80°C oven for 1 hour for full polymerization. These microfibers were cut into pieces of ~0.5 cm in length and hanged between two glass coverslips of 170  $\mu$ m in thickness with a gap of ca. 0.5 to 1 mm, thus avoiding cells on the microfibers getting into contact with the substrate. The whole setup was then stuck to a glass-bottom petri dish (FluoroDish, catalog no. FD35-100) for protein functionalization.

Following the similar procedures as above, soft silicon microtubes and microfibers were made from a mixture of silicon gels 52-276 A and B (Dow Corning) at a ratio of 5:6. The curing time for this soft polymer is 30 to 60 min at room temperature, followed by 1-hour baking at 80°C.

To facilitate cell adhesion, PDMS microtubes and microfibers were first treated with oxygen plasma for 5 min using a plasma cleaner (Harrick Plasma, P/N PDC-002-HPCE). Soft silicon microtubes/fibers were exposed to ultraviolet in a UVO-Cleaner (Jelight Company Inc., model 342-220) for 2 min. All the elastomeric microtubes/fibers were then coated with fibronectin (Sigma-Aldrich) by soaking into a fibronectin solution of 50  $\mu$ g/ml overnight at 4°C. These cylindrical scaffolds were thoroughly rinsed with 1× PBS before cell seeding.

### Formation of MDCK epithelial CTs

To form MDCK *t*-CTs, MDCK cells were seeded right outside both openings of elastomeric microtubes and let migrate into the microtubes freely until confluence. Before the confluence, MDCK cohorts inside microtubes formed advancing, nonconfluent *t*-CTs. It normally took 2 to 3 days to form confluent *t*-CTs, and a complete DMEM containing 10  $\mu$ M mitomycin C (Sigma-Aldrich) was added for 1 hour to block cell division (collective rotation in CTs could also be observed without the treatment of mitomycin C, but blocking mitosis notably increased the percentage of rotation). As-formed *t*-CTs were washed and immersed with/in fresh DMEM and mounted on a confocal microscope (Zeiss, LSM 780 or LSM 980) for 3D live cell imaging.

MDCK *f*-CTs were formed in a similar way by seeding MDCK cells right next to both ends of elastomeric microfibers and let them to migrate onto the microfibers freely until confluence. As-formed *f*-CTs were also treated with 10  $\mu$ M mitomycin C for 1 hour to block mitosis and enhance CeR.

### Live-cell imaging of collective rotation in MDCK CTs and drug treatment

Samples of MDCK CTs were mounted on a confocal microscope (Zeiss, LSM 780 or LSM 980), and *z* stacks (0.5 to 1  $\mu$ m per *Z* step) covering the whole volume of MDCK CTs were recorded at 10 min per frame with either 25 $\times$ , 40 $\times$ , or 63 $\times$  objectives. Alternatively, MDCK CTs were imaged at 10 min per frame with a BioStation

IM-Q (Nikon) using a 10 $\times$  objectives with multiple focal planes to cover the entire MDCK CTs. To facilitate cell tracking, H1-GFP MDCKs or MDCKs expressing LifeAct GFP or YFP-PBD or MDCK myosin-II-RFP were used. Otherwise, nuclei in MDCK WT, E-cad KO, cadherin double KO, or  $\alpha$ -cat KD cells were stained with the NUCLEAR-ID Blue DNA Dye (Enzo, ENZ-CHM103-0200) by mixing 1  $\mu$ l of the dye in 1 ml of DMEM. 3D time-lapse videos were recorded over a period ranging from 12 to 72 hours. During imaging, drug treatment to rotating MDCK CTs was performed. Drugs were added during the course of imaging to allow continuous observations of the effects for 10 to 20 hours. Similarly, washout of drugs using fresh prewarmed complete DMEM was recorded by continuous live-cell imaging that lasted for 10 to 30 hours after. To inhibit Rac-1 activity, cells were treated with 100  $\mu$ M Z62954982 (Merck Millipore, catalog no. CAS 1090893-12-1). For Ca<sup>2+</sup>-dependent adhesion disruption, EGTA (Sigma-Aldrich) was added to make a final concentration of 2.5 mM during experiments and left to react for at least 20 hours. To inhibit cell contractility, ROCK inhibitor Y-27632 (Sigma-Aldrich, Y0503) was added to DMEM to make a final concentration of 10 to 25  $\mu$ M.

### Immunofluorescent staining of MDCK CTs and confocal microscopy

Before cell fixation, live-cell imaging of MDCK CTs was performed using a BioStation IM-Q (Nikon) to spot collective cell rotation in CTs. The rotating CTs were then immediately fixed with 4% paraformaldehyde for 20 min, permeabilized with 0.1% Triton X-100 for 10 min while shaking, and blocked in a solution of 3% bovine serum albumin (BSA) for 2 hours. Antibodies and phalloidin were diluted in 3% BSA solution. Actin cytoskeleton was visualized after staining with either Alexa Fluor 488 (1:250; Invitrogen, A12379)-, Alexa Fluor 568 (1:250; Invitrogen, A12380)-, or Alexa Fluor 647 (1:25; Invitrogen, A22287)-labeled phalloidin for 2 hours. For staining  $\alpha$ - or  $\beta$ -catenin, samples were incubated with either a primary antibody against  $\alpha$ -catenin, raised in rabbit (1:100; Sigma-Aldrich), or a primary antibody against  $\beta$ -catenin, raised in rabbit (1:100; Sigma-Aldrich). For staining the apical side of MDCK CTs, samples were incubated with a primary antibody against GP-135, raised in mouse (1:100; Developmental Studies Hybridoma Bank, 3F2/D8). All samples were incubated overnight with primary antibody solutions at 4°C, while shaking. The next day, a washing procedure of 3 × 10 min using 1× PBS was applied to wash away the extra primary antibodies. Cells were then stained with 1:50 to 1:200 dilutions of secondary antibodies (Invitrogen) and Hoechst 33342 (1:1000; Life Technologies, H3570). Samples were mounted with antibleaching medium (Vector Laboratories, H-1000), and *z* stacks of MDCK CTs were acquired on a confocal microscope (Zeiss LSM980 or LSM780) using a 40 $\times$  or a 25 $\times$  oil or a 63 $\times$  water objective at 0.5 to 1  $\mu$ m per stack.

### Traction force microscopy

TFM (16, 41) was performed to examine traction exerted by MDCK CTs on cylindrical substrates. Briefly, soft silicon microtubes and microfibers were coated with a layer of red fluorescent carboxylate-modified microbeads (Invitrogen, F8810) by silanizing the surfaces using a 10% solution of (3-aminopropyl)triethoxysilane (Sigma-Aldrich, A3648) in 100% ethanol for 15 min. The microbead-laden soft silicon microtubes and microfibers were later coated with fibronectin by direct incubation at a concentration of 50  $\mu$ g/ml overnight at 4°C. MDCK cells were then allowed to form epithelial

CTs on these soft cylindrical substrates. Live-cell imaging was performed on these samples to record bead displacement and CeR simultaneously. At the end of the video, 500  $\mu\text{l}$  of 10% SDS were added in the medium to remove cells to obtain the reference positions of the microbeads. The displacement of microbeads relative to the reference positions was tracked using PIVlab with a PIV interrogation window size of 16 pixels by 16 pixels and an overlap of 50%. We then obtained TFs of rotating CTs from bead displacements using a Fiji plugin FTTC (65) with a regularization parameter of  $9 \times 10^{-9}$ .

To determine the elasticity of Matrigel and soft silicon, atomic force microscopy (AFM) measurements were performed on a JPK NanoWizard III AFM that was mounted on a Zeiss Axio Observer. Z1 optical microscope. Before the measurement, Bruker MLCT-SPH-5UM DC colloidal probes with a tip radius of 5.5  $\mu\text{m}$  were calibrated according to the standardized nanomechanical AFM procedure (SNAP) method. Force mapping covering 90- $\mu\text{m}^2$  arrays of  $8 \times 8$  force curves was performed on the samples. Tip velocity was set to 2  $\mu\text{m/s}$ , and force threshold was set to 10 nN. Data were recorded using the JPK 6.3.43 version and were analyzed with Hertz model using the corresponding data processing software. Gel elasticities are presented as the means  $\pm$  SEM in the results.

### Image analysis

To convert 3D  $z$  stack images of MDCK CTs into 2D projections, we used a Fiji macro described previously (64). Briefly, background subtraction was performed to reduce signal-to-noise ratio. The  $z$  stack images were then resliced to project the  $xz$  plane for the circular cross section of MDCK CTs. Afterward, a circle was fit to the circumference of the  $t$ -CTs/ $f$ -CTs, and their perimeters were mapped into a line, which was straightened and resliced again to obtain a 2D projection of virtually opened  $t$ -CTs/ $f$ -CTs. The circumferences of MDCK CTs became the new azimuthal ( $a$ ) axis, and the length became the new longitudinal ( $l$ ) axis.

For analysis of cell velocity, we performed PIV mapping with PIVlab (a tool implemented using MATLAB R2020) on the obtained 2D time-lapse projections of MDCK H1-GFP 3D movies (21, 64). Nuclei movements were used to match those of the cells. Interrogation windows of 64 pixels by 64 pixels and 32 pixels by 32 pixels with a 50% overlap were applied. Outlier vectors in the acquired mapping were manually removed, and a local SD filter was used. With these settings, we calculated the velocity components in the longitudinal ( $\vec{V}_z$ ) and azimuthal ( $\vec{V}_\theta$ ) directions, and the velocity correlation length,  $\xi$ , was calculated using a formula described previously (66).

To analyze actin filaments/ $\beta$ -catenin finger alignment in MDCK CTs, we calculated the orientation of each filament/finger using OrientationJ (67), a plugin of Fiji. Similarly, we manually lined out cell peripheries in rotating CTs, applied an ellipsoidal fit, and measured their orientations using OrientationJ. The obtained data were plotted with rose diagrams using MATLAB R2020.

### Statistical analysis

Statistical analysis was performed using GraphPad Prism (version 7.00) or Microsoft Excel. All  $P$  values were derived from Student's  $t$  tests comparing two groups using unpaired two-tailed analysis with Welch's correction or paired two-tailed  $t$  tests, unless otherwise noted. Error bars denote the SD. Statistical significance was defined as  $P < 0.05$  with regard to the null hypothesis.

### SUPPLEMENTARY MATERIALS

Supplementary material for this article is available at <https://science.org/doi/10.1126/sciadv.abn5406>

[View/request a protocol for this paper from Bio-protocol.](#)

### REFERENCES AND NOTES

1. S. L. Haigo, D. Bilder, Global tissue revolutions in a morphogenetic movement controlling elongation. *Science* **331**, 1071–1074 (2011).
2. M. Cetera, G. R. Ramirez-San Juan, P. W. Oakes, L. Lewellyn, M. J. Fairchild, G. Tanentzapf, M. L. Gardel, S. Horne-Badovinac, Epithelial rotation promotes the global alignment of contractile actin bundles during *Drosophila* egg chamber elongation. *Nat. Commun.* **5**, 5511 (2014).
3. A. Popkova, O. J. Stone, L. Chen, X. Qin, C. Liu, J. Liu, K. Belguisse, D. J. Montell, K. M. Hahn, M. Rauzi, X. Wang, A Cdc42-mediated supracellular network drives polarized forces and *Drosophila* egg chamber extension. *Nat. Commun.* **11**, 1921 (2020).
4. K. Sato, T. Hiraiwa, E. Maekawa, A. Isomura, T. Shibata, E. Kuranaga, Left-right asymmetric cell intercalation drives directional collective cell movement in epithelial morphogenesis. *Nat. Commun.* **6**, 10074 (2015).
5. K. Tanner, H. Mori, R. Mroue, A. Bruni-Cardoso, M. J. Bissell, Coherent angular motion in the establishment of multicellular architecture of glandular tissues. *Proc. Natl. Acad. Sci. U.S.A.* **109**, 1973–1978 (2012).
6. P. A. Fernández, B. Buchmann, A. Goychuk, L. K. Engelbrecht, M. K. Raich, C. H. Scheel, E. Frey, A. R. Bausch, Surface-tension-induced budding drives alveogenesis in human mammary gland organoids. *Nat. Phys.* **17**, 1130–1136 (2021).
7. J. Zhang, K. F. Goliwas, W. Wang, P. V. Taufalele, F. Bordeleau, C. A. Reinhart-King, Energetic regulation of coordinated leader-follower dynamics during collective invasion of breast cancer cells. *Proc. Natl. Acad. Sci. U.S.A.* **116**, 7867–7872 (2019).
8. H. Wang, S. Lacoche, L. Huang, B. Xue, S. K. Muthuswamy, Rotational motion during three-dimensional morphogenesis of mammary epithelial acini relates to laminin matrix assembly. *Proc. Natl. Acad. Sci. U.S.A.* **110**, 163–168 (2013).
9. P. Rørth, Fellow travellers: Emergent properties of collective cell migration. *EMBO Rep.* **13**, 984–991 (2012).
10. S. Jain, V. M. L. Cachoux, G. H. N. S. Narayana, S. de Beco, J. D'Alessandro, V. Cellerin, T. Chen, M. L. Heuzé, P. Marcq, R.-M. Mège, A. J. Kabla, C. T. Lim, B. Ladoux, The role of single-cell mechanical behaviour and polarity in driving collective cell migration. *Nat. Phys.* **16**, 802–809 (2020).
11. R. Mayor, S. Etienne-Manneville, The front and rear of collective cell migration. *Nat. Rev. Mol. Cell Biol.* **17**, 97–109 (2016).
12. B. Ladoux, R.-M. Mège, Mechanobiology of collective cell behaviours. *Nat. Rev. Mol. Cell Biol.* **18**, 743–757 (2017).
13. M. Reffay, L. Petitjean, S. Coscoy, E. Grasland-Mongrain, F. Amblard, A. Buguin, P. Silberzan, Orientation and polarity in collectively migrating cell structures: Statics and dynamics. *Biophys. J.* **100**, 2566–2575 (2011).
14. R. Farooqui, G. Fentanyi, Multiple rows of cells behind an epithelial wound edge extend cryptic lamellipodia to collectively drive cell-sheet movement. *J. Cell Sci.* **118**, 51–63 (2005).
15. D. J. Montell, Morphogenetic cell movements: Diversity from modular mechanical properties. *Science* **322**, 1502–1505 (2008).
16. X. Trepat, M. R. Wasserman, T. E. Angelini, E. Millet, D. A. Weitz, J. P. Butler, J. J. Fredberg, Physical forces during collective cell migration. *Nat. Phys.* **5**, 426–430 (2009).
17. F. Peglion, F. Llense, S. Etienne-Manneville, Adherens junction treadmilling during collective migration. *Nat. Cell Biol.* **16**, 639–651 (2014).
18. K. M. Sherrard, M. Cetera, S. Horne-Badovinac, DAAM mediates the assembly of long-lived, treadmilling stress fibers in collectively migrating epithelial cells in *Drosophila*. *bioRxiv* 2021.08.2027.455521 [Preprint]. 8 August 2021. <https://doi.org/10.1101/2021.08.07.455521>.
19. T. Chen, A. Callan-Jones, E. Fedorov, A. Ravasio, A. Brugués, H. T. Ong, Y. Toyama, B. C. Low, X. Trepat, T. Shemesh, R. Voituriez, B. Ladoux, Large-scale curvature sensing by directional actin flow drives cellular migration mode switching. *Nat. Phys.* **15**, 393–402 (2019).
20. Y. Y. Biton, S. A. Safran, The cellular response to curvature-induced stress. *Phys. Biol.* **6**, 046010 (2009).
21. W. Xi, S. Sonam, T. Beng Saw, B. Ladoux, C. Teck Lim, Emergent patterns of collective cell migration under tubular confinement. *Nat. Commun.* **8**, 1517 (2017).
22. H. G. Yevick, G. Duclos, I. Bonnet, P. Silberzan, Architecture and migration of an epithelium on a cylindrical wire. *Proc. Natl. Acad. Sci. U.S.A.* **112**, 5944–5949 (2015).
23. Y. Maroudas-Sacks, L. Garion, L. Shani-Zerbib, A. Livshits, E. Braun, K. Keren, Topological defects in the nematic order of actin fibres as organization centres of *Hydra* morphogenesis. *Nat. Phys.* **17**, 251–259 (2021).
24. M. Gupta, B. R. Sarangi, J. Deschamps, Y. Nematbakhsh, A. Callan-Jones, F. Margadant, R.-M. Mège, C. T. Lim, R. Voituriez, B. Ladoux, Adaptive rheology and ordering of cell cytoskeleton govern matrix rigidity sensing. *Nat. Commun.* **6**, 7525 (2015).

25. D. J. G. Pearce, S. Gat, G. Livne, A. Bernheim-Grosbawer, K. Kuruse, Defect-driven shape transitions in elastic active nematic shells. arXiv:2010.13141 [cond-mat.soft] (25 October 2020).
26. L. A. Hoffmann, L. N. Carenza, J. Eckert, L. Giomi, Theory of defect-mediated morphogenesis. *Sci. Adv.* **8**, eabk2712 (2022).
27. I. Nitschke, S. Reuther, A. Voigt, Liquid crystals on deformable surfaces. *Proc. R. Soc. A Math. Phys. Eng. Sci.* **476**, 20200313 (2020).
28. A. S. Chin, K. E. Worley, P. Ray, G. Kaur, J. Fan, L. Q. Wan, Epithelial cell chirality revealed by three-dimensional spontaneous rotation. *Proc. Natl. Acad. Sci. U.S.A.* **115**, 12188–12193 (2018).
29. D. T. Tambe, C. Corey Hardin, T. E. Angelini, K. Rajendran, C. Y. Park, X. Serra-Picamal, E. H. Zhou, M. H. Zaman, J. P. Butler, D. A. Weitz, J. J. Fredberg, X. Trepaut, Collective cell guidance by cooperative intercellular forces. *Nat. Mater.* **10**, 469–475 (2011).
30. P. Leroy, K. E. Mostov, Slug is required for cell survival during partial epithelial-mesenchymal transition of HGF-induced tubulogenesis. *Mol. Biol. Cell* **18**, 1943–1952 (2007).
31. T. Hirashima, M. Hoshuyama, T. Adachi, In vitro tubulogenesis of Madin-Darby canine kidney (MDCK) spheroids occurs depending on constituent cell number and scaffold gel concentration. *J. Theor. Biol.* **435**, 110–115 (2017).
32. S. Horne-Badovinac, D. Bilder, Mass transit: Epithelial morphogenesis in the drosophila egg chamber. *Dev. Dyn.* **232**, 559–574 (2005).
33. A. Doostmohammadi, S. P. Thampi, T. B. Saw, C. T. Lim, B. Ladoux, J. M. Yeomans, Celebrating soft matter's 10th anniversary: Cell division: A source of active stress in cellular monolayers. *Soft Matter* **11**, 7328–7336 (2015).
34. R. W. Naylor, H.-H. G. Chang, S. Qubisi, A. J. Davidson, A novel mechanism of gland formation in zebrafish involving transdifferentiation of renal epithelial cells and live cell extrusion. *eLife* **7**, e38911 (2018).
35. F. Martin-Belmonte, K. Mostov, Regulation of cell polarity during epithelial morphogenesis. *Curr. Opin. Cell Biol.* **20**, 227–234 (2008).
36. J. d'Alessandro, A. Barbier-Chebbah, V. Cellierin, O. Benichou, R. M. Mège, R. Voituriez, B. Ladoux, Cell migration guided by long-lived spatial memory. *Nat. Commun.* **12**, 4118 (2021).
37. S. R. K. Vedula, M. C. Leong, T. L. Lai, P. Hersen, A. J. Kabla, C. T. Lim, B. Ladoux, Emerging modes of collective cell migration induced by geometrical constraints. *Proc. Natl. Acad. Sci. U.S.A.* **109**, 12974–12979 (2012).
38. L. Balasubramaniam, A. Doostmohammadi, T. B. Saw, G. H. N. S. Narayana, R. Mueller, T. Dang, M. Thomas, S. Gupta, S. Sonam, A. S. Yap, Y. Toyama, R.-M. Mège, J. M. Yeomans, B. Ladoux, Investigating the nature of active forces in tissues reveals how contractile cells can form extensible monolayers. *Nat. Mater.* **20**, 1156–1166 (2021).
39. R. Sunyer, V. Conte, J. Escrivano, A. Elosegi-Artola, A. Labernadie, L. Valon, D. Navajas, J. M. García-Aznar, J. J. Muñoz, P. Roca-Cusachs, X. Trepaut, Collective cell durotaxis emerges from long-range intercellular force transmission. *Science* **353**, 1157–1161 (2016).
40. W. Xi, T. B. Saw, D. Delacour, C. T. Lim, B. Ladoux, Material approaches to active tissue mechanics. *Nat. Rev. Mater.* **4**, 23–44 (2019).
41. A. Ravasio, I. Cheddadi, T. Chen, T. Pereira, H. T. Ong, C. Bertocchi, A. Brugues, A. Jacinto, A. J. Kabla, Y. Toyama, X. Trepaut, N. Gov, L. Neves de Almeida, B. Ladoux, Gap geometry dictates epithelial closure efficiency. *Nat. Commun.* **6**, 7683 (2015).
42. M. Luciano, S.-L. Xue, W. H. De Vos, L. Redondo-Morata, M. Surin, F. Lafont, E. Hannezo, S. Gabriele, Cell monolayers sense curvature by exploiting active mechanics and nuclear mechanoadaptation. *Nat. Phys.* **17**, 1382–1390 (2021).
43. L. Pieuchot, J. Marteau, A. Guignandon, T. Dos Santos, I. Brigaud, P.-F. Chauvy, T. Cloatre, A. Ponche, T. Petithory, P. Rougerie, M. Vassaux, J.-L. Milan, N. Tusamda Wakhloo, A. Spangenberg, M. Bigerelle, K. Anselme, Curvotaxis directs cell migration through cell-scale curvature landscapes. *Nat. Commun.* **9**, 3995 (2018).
44. P. Rougerie, L. Pieuchot, R. S. dos Santos, J. Marteau, M. Bigerelle, P.-F. Chauvy, M. Farina, K. Anselme, Topographical curvature is sufficient to control epithelium elongation. *Sci. Rep.* **10**, 14784 (2020).
45. S.-M. Yu, J. M. Oh, J. Lee, W. Lee-Kwon, W. Jung, F. Amblard, S. Granick, Y.-K. Cho, Substrate curvature affects the shape, orientation, and polarization of renal epithelial cells. *Acta Biomater.* **77**, 311–321 (2018).
46. I. D. Johnston, D. K. McCluskey, C. K. L. Tan, M. C. Tracey, Mechanical characterization of bulk Sylgard 184 for microfluidics and microengineering. *J. Micromech. Microeng.* **24**, 035017 (2014).
47. L. Lu, S. J. Oswald, H. Ngu, F. C. Yin, Mechanical properties of actin stress fibers in living cells. *Biophys. J.* **95**, 6060–6071 (2008).
48. C. S. Chen, J. Tan, J. Tien, Mechanotransduction at cell-matrix and cell-cell contacts. *Annu. Rev. Biomed. Eng.* **6**, 275–302 (2004).
49. M. Bienz,  $\beta$ -Catenin: A pivot between cell adhesion and wnt signalling. *Curr. Biol.* **15**, R64–R67 (2005).
50. K. A. Knudsen, A. P. Soler, K. R. Johnson, M. J. Wheelock, Interaction of alpha-actinin with the cadherin/catenin cell-cell adhesion complex via alpha-catenin. *J. Cell Biol.* **130**, 67–77 (1995).
51. S. Yonemura, Y. Wada, T. Watanabe, A. Nagafuchi, M. Shibata,  $\alpha$ -Catenin as a tension transducer that induces adherens junction development. *Nat. Cell Biol.* **12**, 533–542 (2010).
52. M. Rauzi, P. Verant, T. Lecuit, P.-F. Lenne, Nature and anisotropy of cortical forces orienting Drosophila tissue morphogenesis. *Nat. Cell Biol.* **10**, 1401–1410 (2008).
53. K. Matsuzawa, T. Himoto, Y. Mochizuki, J. Ikenouchi,  $\alpha$ -Catenin controls the anisotropy of force distribution at cell-cell junctions during collective cell migration. *Cell Rep.* **23**, 3447–3456 (2018).
54. W. Y. Wang, C. D. Davidson, D. Lin, B. M. Baker, Actomyosin contractility-dependent matrix stretch and recoil induces rapid cell migration. *Nat. Commun.* **10**, 1186 (2019).
55. S. Jain, B. Ladoux, R. M. Mège, Mechanical plasticity in collective cell migration. *Curr. Opin. Cell Biol.* **72**, 54–62 (2021).
56. C. Blanch-Mercader, R. Vincent, E. Bazellières, X. Serra-Picamal, X. Trepaut, J. Casademunt, Effective viscosity and dynamics of spreading epithelia: A solvable model. *Soft Matter* **13**, 1235–1243 (2017).
57. K. Kruse, J. F. Joanny, F. Jülicher, J. Prost, K. Sekimoto, Generic theory of active polar gels: A paradigm for cytoskeletal dynamics. *Eur. Phys. J. E* **16**, 5–16 (2005).
58. F. Jülicher, K. Kruse, J. Prost, J. F. Joanny, Active behavior of the cytoskeleton. *Phys. Rep.* **449**, 3–28 (2007).
59. M. Poujade, E. Grasland-Mongrain, A. Hertzog, J. Jouanneau, P. Chavrier, B. Ladoux, A. Buguin, P. Silberzan, Collective migration of an epithelial monolayer in response to a model wound. *Proc. Natl. Acad. Sci. U.S.A.* **104**, 15988–15993 (2007).
60. T. E. Angelini, E. Hannezo, X. Trepaut, M. Marquez, J. J. Fredberg, D. A. Weitz, Glass-like dynamics of collective cell migration. *Proc. Natl. Acad. Sci. U.S.A.* **108**, 4714–4719 (2011).
61. J. M. López-Gay, H. Nunley, M. Spencer, F. di Pietro, B. Guirao, F. Bosveld, O. Markova, I. Gaugue, S. Pelletier, D. K. Lubensky, Y. Bellaïche, Apical stress fibers enable a scaling between cell mechanical response and area in epithelial tissue. *Science* **370**, eabb2169 (2020).
62. P. Haas, D. Gilmour, Chemokine signaling mediates self-organizing tissue migration in the zebrafish lateral line. *Dev. Cell* **10**, 673–680 (2006).
63. Q. Guo, B. Xia, S. Moshiach, C. Xu, Y. Jiang, Y. Chen, Y. Sun, J. M. Lahti, X. A. Zhang, The microenvironmental determinants for kidney epithelial cyst morphogenesis. *Eur. J. Cell Biol.* **87**, 251–266 (2008).
64. W. Xi, S. Sonam, C. T. Lim, B. Ladoux, in *Methods in Cell Biology*, J. Doh, D. Fletcher, M. Piel, Eds. (Academic Press, 2018), vol. 146, pp. 3–21.
65. Q. Tseng, E. Duchemin-Pelletier, A. Deshiere, M. Balland, H. Guillou, O. Filhol, M. Théry, Spatial organization of the extracellular matrix regulates cell–cell junction positioning. *Proc. Natl. Acad. Sci. U.S.A.* **109**, 1506–1511 (2012).
66. L. Petitjean, M. Reffay, E. Grasland-Mongrain, M. Poujade, B. Ladoux, A. Buguin, P. Silberzan, Velocity fields in a collectively migrating epithelium. *Biophys. J.* **98**, 1790–1800 (2010).
67. Z. Püspöki, M. Storath, D. Sage, M. Unser, Transforms and operators for directional bioimage analysis: A survey. *Adv. Anat. Embryol. Cell Biol.* **219**, 69–93 (2016).
68. G. Napoli, L. Vergori, Extrinsic curvature effects on nematic shells. *Phys. Rev. Lett.* **108**, 207803 (2012).
69. G. Napoli, L. Vergori, Surface free energies for nematic shells. *Phys. Rev. E* **85**, 061701 (2012).
70. A. Segatti, M. Snarski, M. Veneroni, Equilibrium configurations of nematic liquid crystals on a torus. *Phys. Rev. E* **90**, 012501 (2014).
71. D. Jesenek, S. Kralj, R. Rosso, E. G. Virga, Defect unbinding on a toroidal nematic shell. *Soft Matter* **11**, 2434–2444 (2015).
72. I. Nitschke, M. Nestler, S. Praetorius, H. Löwen, A. Voigt, Nematic liquid crystals on curved surfaces: A thin film limit. *Proc. R. Soc. A Math. Phys. Eng. Sci.* **474**, 20170686 (2018).
73. M. Nestler, I. Nitschke, S. Praetorius, A. Voigt, Orientational order on surfaces: The coupling of topology, geometry, and dynamics. *J. Nonlinear Sci.* **28**, 147–191 (2018).
74. M. Nestler, I. Nitschke, H. Löwen, A. Voigt, Properties of surface Landau-de Gennes Q-tensor models. *Soft Matter* **16**, 4032–4042 (2020).
75. D. J. G. Pearce, P. W. Ellis, A. Fernandez-Nieves, L. Giomi, Geometrical control of active turbulence in curved topographies. *Phys. Rev. Lett.* **122**, 168002 (2019).
76. D. J. G. Pearce, Defect order in active nematics on a curved surface. *New J. Phys.* **22**, 063051 (2020).
77. D. Khoromskaia, G. Salbreux, Active morphogenesis of patterned epithelial shells. arXiv:2111.12820 [physics.bio-ph] (24 November 2021).
78. M. Nestler, A. Voigt, Active nematodynamics on curved surfaces—The influence of geometri forces on motion patterns of topological defects. arXiv:2107.07779 [cond-mat.soft] (1 July 2021).
79. G. Salbreux, F. Jülicher, J. Prost, A. Callan-Jones, Theory of nematic and polar active fluid surfaces. arXiv:2201.09251 [cond-mat.soft] (23 January 2022).
80. S. Bell, S.-Z. Lin, J.-F. Rupprecht, J. Prost, Active nematic flows on curved surfaces. arXiv:2203.05644 [physics.bio-ph] (10 March 2022).
81. P. G. de Gennes, J. Prost, *The Physics of Liquid Crystals* (Clarendon Press, 1993).

82. M. Nestler, I. Nitschke, A. Voigt, A finite element approach for vector- and tensor-valued surface PDEs. *J. Comput. Phys.* **389**, 48–61 (2019).
83. M. C. Marchetti, J. F. Joanny, S. Ramaswamy, T. B. Liverpool, J. Prost, M. Rao, R. A. Simha, Hydrodynamics of soft active matter. *Rev. Mod. Phys.* **85**, 1143–1189 (2013).

**Acknowledgments:** We thank the group members from the “Cell adhesion and migration” team at the Institut Jacques Monod (IJM) for helpful discussions. We are indebted to T. Nguyen and O. Frenoy for support during biological experiments and generating MDCK cadherin double KO cells and to F. Kong (NUS, Singapore) for help in microfabrication. We are thankful to R.-M. Mege for inspiring discussions. We acknowledge the ImagoSeine core facility of IJM, member of IBISA, the imaging facility MRI, member of the France-Biolimaging infrastructures (ANR-10-INBS-04, “Investment for the future”), and the microscopy core of Mechanobiology Institute Singapore for imaging support. We also acknowledge the aquatic facility of the CRBM, N. Taulet for help with zebrafish experimental developments and in vivo movie processing, and P. Richard and M. Plays for zebrafish husbandry. **Funding:** This work was supported by the LABEX “Who Am I?” (ANR-11-LABX-0071) (to B.L.); the European Research Council (ERC) (grant no. Adv-101019835) (to B.L.); the Marie Skłodowska-Curie Actions, Individual Fellowship, project 846449 (to W.X.); People Programme (Marie Curie Actions) of the European Union’s Seventh Framework Programme (FP7/2007–2013) under REA grant agreement no. PCOFUND-GA-2013-609102, through the PRESTIGE program coordinated by Campus France (to W.X.); funding from the Labex Who Am I? (ANR-11-LABX-0071) and the “Initiatives d’excellence” (Idex ANR-11-IDEX-0005-02) transverse project BioMechanOE (TP5) (to W.X.); the Agence Nationale de la Recherche (ANR) “POLCAM” ANR-17-CE13-0013 funded

by the French government (to B.L.); the SystemsX EpiPhysX consortium funding (to C.B.-M.); the NR PRC LUCELL grant (ANR-19-CE13-0014-01) (to B.D.); the ANR-10-EQPX-04-01 (to F.L.); the European Regional Development Fund (FEDER-12001407) (to F.L.); the Groupama Foundation—Research Prize for Rare Diseases 2017 (to D.D. and W.X.); the ANR “LUCELL” ANR-19-CE13-0014 funded by the French government (to B.D. and D.D.); the Fondation pour la Recherche Médicale (FRM) (to D.D.); the Université de Paris IDEX, ANR-18-IDEX-0001, funded by the French government through its “Investments for the Future” program (to D.D.); the Human Frontier Science Program, RGP0038/2018 (to D.D., C.T.L., T.B.S., J.P., and W.X.); Lee Kuan Yew Postdoctoral fellowship and Tier 1 grant (R-397-000-320-114) from the Ministry of Education (MOE), Singapore (to T.B.S.); and the National Research Foundation, Singapore, under the Mechanobiology Institute at the National University of Singapore (to C.T.L.).

**Author contributions:** Conceptualization: W.X., B.L., and J.P. Methodology: W.X., B.L., A.G., J.P., C.B.-M., T.B.S., and C.T.L. Investigation: A.G., C.B.-M., W.X., D.D., L.B., S.J., F.L., A.D., and B.D. Analysis: A.G., L.B., C.B.-M., W.X., J.D., and T.B.S. Visualization: A.G., W.X., and C.B.M. Supervision: W.X., B.L., and J.P. Writing—original draft: A.G., C.B.-M., and W.X. Writing—review and editing: W.X., B.L., J.P., and C.B.M. **Competing interests:** The authors declare that they have no competing interests. **Data and materials availability:** All data needed to evaluate the conclusions in the paper are present in the paper and/or the Supplementary Materials.

Submitted 3 December 2021

Accepted 29 July 2022

Published 14 September 2022

10.1126/sciadv.abn5406